Title

TYPE II SUPERNOVA ENERGETICS AND COMPARISON OF LIGHT CURVES TO SHOCK-COOLING MODELS

Authors

Rubin, Adam

Gal-Yam, Avishay

De, Annalisa

et al.

Peer reviewed

TYPE II SUPERNOVA ENERGETICS AND COMPARISON OF LIGHT CURVES TO SHOCK-COOLING MODELS

Adam Rubin,[1] Avishay Gal-Yam,[1] Annalisa De Cia,[1] Assaf Horesh,[1] Danny Khazov,[1] Eran O. Ofek,[1] S. R. Kulkarni,[2,3] Iair Arcavi,[4,5] Ilan Manulis,[1] Ofer Yaron,[1] Paul Vreeswijk,[1] Mansi M. Kasliwal,[6] Sagi Ben-Ami,[7] Daniel A. Perley,[2,8] Yi Cao,[2] S. Bradley Cenko,[9,10] Umaa D. Rebbapragada,[11] P. R. Woźniak,[12] Alexei V. Filippenko,[13] K. I. Clubb,[13] Peter E. Nugent,[13,14] Y.-C. Pan,[15] C. Badenes,[16] D. Andrew Howell,[4,17] Stefano Valenti,[4] David Sand,[18] J. Sollerman,[19] Joel Johansson,[20] Douglas C. Leonard,[21] J. Chuck Horst,[21] Stephen F. Armen,[21] Joseph M. Fedrow,[21,22] Robert M. Quimby,[21,23] Paulo Mazzali,[24,25] Elena Pian,[26,27] Assaf Sternberg,[25,28] Thomas Matheson,[29] M. Sullivan,[30] K. Maguire,[31] and Sanja Lazarevic[32]

ABSTRACT

During the first few days after explosion, Type II supernovae (SNe) are dominated by relatively simple physics. Theoretical predictions regarding early-time SN light curves in the ultraviolet (UV) and optical bands are thus quite robust. We present, for the first time, a sample of 57 R-band Type II SN light curves that are well monitored during their rise, having > 5 detections during the first 10 days after discovery, and a well-constrained time of explosion to within 1–3 days. We show that the energy per unit mass (E/M) can be deduced to roughly a factor of five by comparing early-time optical data to the model of Rabinak & Waxman (2011), while the progenitor radius cannot be determined based on R-band data alone. We find that Type II SN explosion energies span a range of $E/M = (0.2 - 20) \times 10^{51}$ erg/(10 $M_\odot$), and have a mean energy per unit mass of $\langle E/M \rangle = 0.85 \times 10^{51}$ erg/(10 $M_\odot$), corrected for Malmquist bias. Assuming a small spread in progenitor masses, this indicates a large intrinsic diversity in explosion energy. Moreover, E/M is positively correlated with the amount of ^{56}Ni produced in the explosion, as predicted by some recent models of core-collapse SNe. We further present several empirical correlations. The peak magnitude is correlated with the decline rate (Δm_{15}), the decline rate is weakly correlated with the rise time, and the rise time is not significantly correlated with the peak magnitude. Faster declining SNe are more luminous and have longer rise times. This limits the possible power sources for such events.

[1] Department of Particle Physics and Astrophysics, Weizmann Institute of Science, 234 Herzl St., Rehovot, Israel; adam.rubin@weizmann.ac.il

[2] Astronomy Department, California Institute of Technology, Pasadena, CA 91125, USA

[3] Caltech Optical Observatories, California Institute of Technology, Pasadena, CA 91125, USA

[4] Las Cumbres Observatory Global Telescope Network, 6740 Cortona Dr., Suite 102, Goleta, CA 93117, USA

[5] Kavli Institute for Theoretical Physics, University of California, Santa Barbara, CA 93106, USA

[6] Observatories of the Carnegie Institution for Science, 813 Santa Barbara Street, Pasadena, CA 91101, USA

[7] Smithsonian Astrophysical Observatory, Harvard-Smithsonian Center for Astrophysics, 60 Garden St., Cambridge, MA 02138, USA

[8] Dark Cosmology Centre, Niels Bohr Institute, University of Copenhagen, Juliane Maries Vej 30, DK-2100 København Ø, Denmark

[9] Astrophysics Science Division, NASA Goddard Space Flight Center, Mail Code 661, Greenbelt, MD 20771, USA

[10] Joint Space Science Institute, University of Maryland, College Park, MD 20742, USA

[11] Jet Propulsion Laboratory, California Institute of Technology, Pasadena, CA 91109, USA

[12] Los Alamos National Laboratory, Los Alamos, NM 87545, USA

[13] Department of Astronomy, University of California, Berkeley, CA 94720-3411, USA

[14] Lawrence Berkeley National Laboratory, Berkeley, CA 94720, USA

[15] Astronomy Department, University of Illinois at Urbana-Champaign, 1002 W. Green Street, Urbana, IL 61801, USA

[16] Department of Physics and Astronomy, and Pittsburgh Particle Physics, Astrophysics, and Cosmology Center (PITT-PACC), University of Pittsburgh, 3941 O'Hara St., Pittsburgh, PA 15260, USA

[17] Department of Physics, University of California, Santa Barbara, Broida Hall, Mail Code 9530, Santa Barbara, CA 93106-9530, USA

[18] Physics Department, Texas Tech University, Lubbock, TX 79409, USA

[19] The Oskar Klein Centre, Department of Astronomy, Stockholm University, SE-106 91 Stockholm, Sweden

[20] The Oskar Klein Centre, Department of Physics, Stockholm University, SE-106 91 Stockholm, Sweden

[21] Department of Astronomy, San Diego State University, San Diego, CA 92182-1221, USA

[22] Yukawa Institute for Theoretical Physics, Kyoto University, Kyoto 606-8502, Japan

[23] Kavli IPMU (WPI), UTIAS, The University of Tokyo, Kashiwa, Chiba, 277-8583, Japan

[24] Astrophysics Research Institute, Liverpool John Moores University, IC2, Liverpool Science Park, 146 Browlow Hill, Liverpool L3 5RF, UK

[25] Max-Planck-Institut für Astrophysik, Karl-Schwarzschild-Strasse 1, D-85748 Garching, Germany

[26] INAF, Institute of Space Astrophysics and Cosmic Physics, via P. Gobetti 101, 40129 Bologna, Italy

[27] Scuola Normale Superiore, Piazza dei Cavalieri 7, I-56126 Pisa, Italy

[28] Excellence Cluster Universe, Technische Universitat München, Boltzmannstr. 2, D-85748 Garching, Germany

[29] National Optical Astronomy Observatory, 950 N. Cherry Avenue, Tucson, AZ 85719, USA

[30] School of Physics and Astronomy, University of Southampton, Southampton SO17 1BJ, UK

[31] ESO, Karl-Schwarzschild-Str. 2, D-85748 Garching, Germany

[32] Department of Astronomy, Faculty of Mathematics, University of Belgrade, Serbia

1. INTRODUCTION

Despite the recent availability of large samples of Type II SN light curves (e.g., Arcavi et al. 2012; Anderson et al. 2014; Faran et al. 2014a,b; Sanders et al. 2015; González-Gaitán et al. 2015), there is little high-quality data in the literature against which to test predictions (e.g., Nakar & Sari 2010; Rabinak & Waxman 2011, NS10, RW11) regarding early-time light-curve behavior in the ultraviolet (UV) and optical bands. Rabinak & Waxman (2011) showed that it is possible to deduce the progenitor star radius (R_*) and energy per unit mass (E/M) from the early UV light curve. This is because at early times (in the first 3–4 days after explosion), the light curve is dominated by shock cooling; the photosphere is at the outer edge of the ejecta, and no recombination has set in. RW11 models describe well the handful of available early UV SN light curves (Soderberg et al. 2008; Gezari et al. 2008; Schawinski et al. 2008), and can fit the rate of UV detections by a GALEX/PTF survey (Ganot et al. 2014).

Recently, Gall et al. (2015) and González-Gaitán et al. (2015) compared large samples of SN II light curves to RW11/NS10 shock-cooling models. Both papers compared SN rise times to rise times derived from shock-cooling models: Gall et al. (2015) used r-band data, while González-Gaitán et al. (2015) compared multi-band photometry. Both papers concluded that only models with small radii are consistent with the data — a conclusion that is in tension with the known association of red supergiants (RSGs) with Type II-P SNe (Smartt et al. 2009). However, as we show in Section 5, comparing to models based on their rise time requires the application of the models beyond their validity and leads to rejection of models with larger radii that fit the early-time data well. Valenti et al. (2014) and Bose et al. (2015) compared multi-band photometry of SN 2013ej and SN 2013ab to RW11 models, but limited their analysis to the first week after explosion. They found their data to be consistent with RW11 models with radii of 400–600 $R_\odot$ and 450–1500 $R_\odot$, respectively.

Basic empirical relations involving the time scales of the rising light curve have yet to be established. This is due to the fact that most of the published SN photometry begins shortly prior to the peak (if at all); light curves that are well sampled during the first days after explosion are still rare. Based on three such events, Gal-Yam et al. (2011) suggested that there may be a trend where more luminous SNe II-P also rise more slowly. More recently, Faran et al. (2014a) suggested that the rise time and luminosity are uncorrelated, but did not perform a quantitative analysis owing to their small sample size. Gall et al. (2015) studied the rise times of 19 well-monitored SNe, and concluded that there is a qualitative trend between rise time and peak magnitude, with brighter events having longer rise times. Here we use a sample of 57 spectroscopically confirmed SN II R-band light curves that were well monitored during their rise to test and establish such correlations, and we quantitatively compare 33 of these to shock-cooling models.

2. THE SAMPLE

Our sample consists of 57 SNe from the Palomar Transient Factory (PTF; Law et al. 2009; Rau et al. 2009) and the intermediate Palomar Transient Factory (iPTF; Kulkarni 2013) surveys. Data were routinely collected by the Palomar 48-inch survey telescope in the Mould R band (Law et al. 2009). Follow-up observations were conducted mainly with the robotic 60-inch telescope (Cenko et al. 2006) using an SDSS r-band filter, with additional telescopes providing supplementary photometry and spectroscopy (see Gal-Yam et al. 2011). We chose SNe that show hydrogen lines in their spectra (Type II), but do not show narrow emission lines at late times (Type IIn; Schlegel 1990; Filippenko 1997; Kiewe et al. 2012). This was done primarily because the optical emission from interacting SNe IIn is dominated by their surrounding medium, and we are interested in the physics of the exploding star itself. We rejected transitional Type IIb SNe that develop strong He I lines and resemble SNe Ib. We also selected only SNe that had (1) at least five detections within ten days of the first detection, (2) well-sampled peaks/plateaus, and (3) an estimated date of explosion determined to within 3 days.

The full list of SNe, their coordinates, and classification spectra is presented in Table 1. Most of the spectra were obtained with the Double Spectrograph (Oke & Gunn 1982) on the 5-m Hale telescope at Palomar Observatory, the Kast spectrograph (Miller & Stone 1993) on the Shane 3-m telescope at Lick Observatory, the Low Resolution Imaging Spectrometer (LRIS; Oke et al. 1995) on the Keck-1 10-m telescope, and the DEep Imaging Multi-Object Spectrograph (DEIMOS; Faber et al. 2003) on the Keck-2 10-m telescope. Spectral reductions followed standard techniques (e.g., Matheson et al. 2000; Silverman et al. 2012). All spectra are publicly available via the Weizmann Interactive Supernova Data Repository (WISeREP, Yaron & Gal-Yam 2012).

The redshift (z) range is 0.0026–0.093, with a median value of 0.03. The distribution of redshifts is given in Figure 1. Note that this is a flux-limited survey, and is unbiased with respect to host galaxy. Some of the events in our sample briefly showed narrow emission lines which vanished after a few days. These are interpreted as "flash-ionization events" (Gal-Yam et al. 2014; Khazov et al. 2015, submitted). All of the photometry is available in the online material.

Arcavi et al. (2014) identified PTF10iam and PTF10nuj as abnormal transients. They were therefore discarded from the sample, leaving 57 events. All remaining objects had typical SN II spectra. Three objects in the sample were difficult to classify but were ultimately retained. We compared the spectrum of PTF10uls and PTF12krf to templates using SNID (Blondin & Tonry 2007). We found that PTF10uls is consistent with a SN II-P spectrum (Figure 2), while PTF12krf is consistent with a SN II-P, though we cannot rule out that it is a SN IIb (Figure 3). The spectrum of iPTF14ajq had significant galaxy contamination. Figure 4 shows the spectrum after subtraction of an Sb1 template (Kinney et al. 1996); it is that of a reddened SN II.
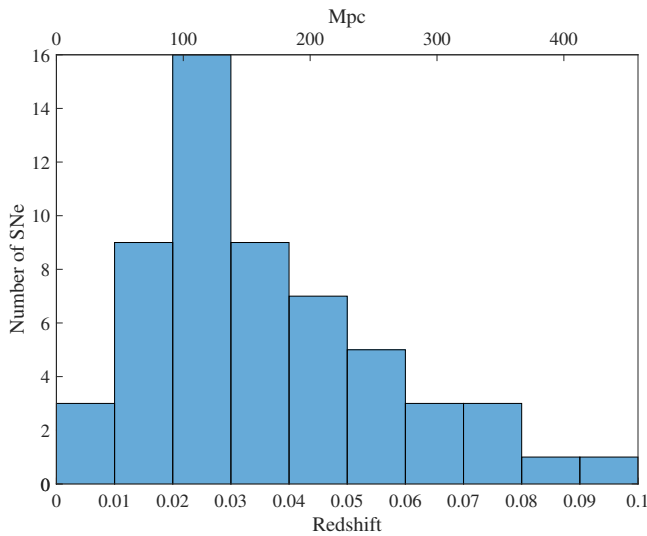
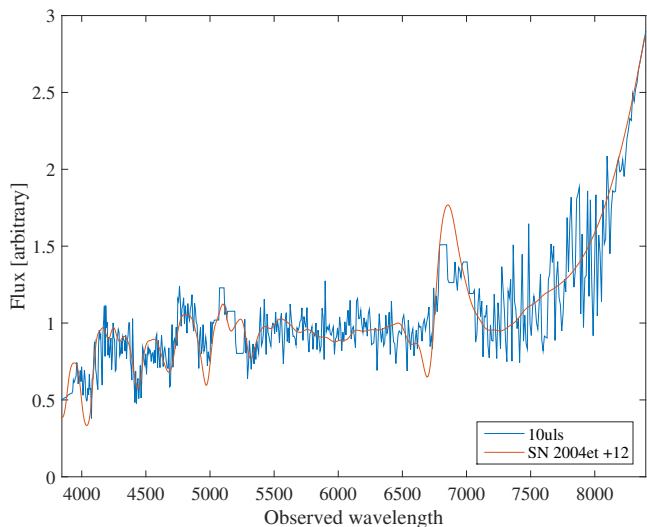**Figure 1.** Redshift distribution of the SNe in the sample.

Figure 2. Spectrum of PTF10uls. Superimposed is the spectrum of SN 2004et (12 days after peak).

Figure 3. Spectrum of PTF12krf. Superimposed are the spectra of Type IIb SN 1993J (2 days before peak) and Type II-P SN 2004et (20 days after peak). Note the weaker He I line compared to SN IIb 1993J.

Figure 4. Subtraction of an Sb1 template from the spectrum of iPTF14ajq. The hydrogen Balmer series is shown offset by 12,000 km s^{-1}.

3. ANALYSIS

3.1. *Photometry*

The photometry was extracted using a point-spread function (PSF) fitting routine (Sullivan et al. 2006; Firth et al. 2015) applied after image subtraction. Photometry for iPTF13dkk, iPTF13dqy (Yaron et al. 2015; submitted to Nature Physics), and iPTF13dzb was supplemented with data from the Las Cumbres Observatory Global Telescope Network (LCOGT; Brown et al. 2013). This was obtained by PSF fitting, and fitting a low-order polynomial to the background. Photometry for PTF12cod was supplemented with data from the 40-inch telescope at Mount Laguna Observatory (MLO), which was also obtained with PSF fitting; see Smith et al. (2015) for details on the MLO reduction procedure. Photometry for PTF10vdl (SN 2010id) was supplemented with that published by Gal-Yam et al. (2011), photometry for PTF12bvh (SN 2012aw) was supplemented with that published by Munari et al. (2013), and photometry for PTF13aaz (SN 2013am) was supplemented with that
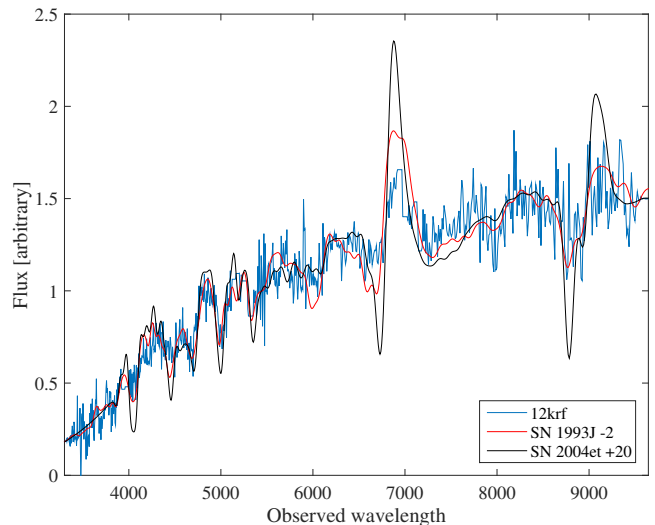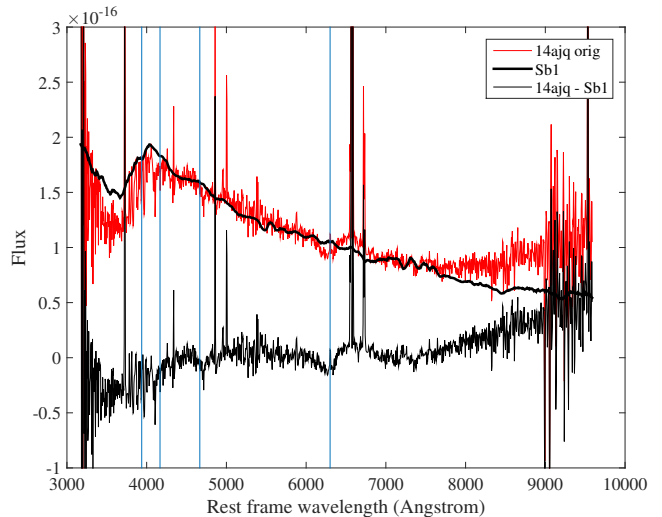
published by Zhang et al. (2014).

The light curves are presented in Appendix Figures B1—B4. We found that small additive constants (indicated in the figures) are needed to bring the supplementary and the 60-inch data in line with the PTF 48-inch observations; this is due most likely to the different r/R filter responses of the 48-inch, 60-inch, and other data sources. The photometry was corrected for Galactic extinction using the Schlegel et al. (1998) maps.[33] The distance moduli were calculated from the spectroscopic redshifts of the host galaxies using a cosmological model with $H_0 = 70$ km s^{-1} Mpc^{-1}, $\Omega_m = 0.3$, and $\Omega_\Lambda = 0.7$. The analysis presented made use of the MATLAB® package for astronomy and astrophysics (Ofek 2014).

The sample was not corrected for local host-galaxy extinction. Faran et al. (2014a) explored various dust-

---

[33] Derived using the *sky_ebv* routine in MATLAB, with $R_V = 3.08$.

extinction correction techniques including photometric methods based on comparison to low-extinction SNe, as well as spectroscopic methods using the Na D doublet equivalent width. They found that none of the procedures increased the uniformity of their sample, and in some cases even increased the scatter. Thus, we would be introducing more uncertainty by correcting according to the classical prescriptions. However, we inspected the sample and found only five questionable objects. PTF09cjq has a red continuum, Na D absorption lines, and likely suffers from extinction. PTF10bgl and iPTF14ajq have a red continuum, but no Na D absorption lines, and may suffer from extinction. PTF10uqn, iPTF13bld, and iPTF13akg have a blue continuum, but show clear Na D absorption lines, and may possibly suffer from extinction — but this is unlikely to be significant, and it may be caused by host contamination in the spectra.

The time of explosion for most objects was estimated as the midpoint between the last non-detection and the first detection. For PTF09ecm, PTF10bgl, PTF10umz, PTF11iqb, PTF12efk, PTF12hsx, iPTF13cly, iPTF14adz, and iPTF14aoi — where the limits were poorer, but the rise was well sampled — we estimated the time of explosion with an exponential fit described in Section A. The fits are shown in Appendix Figure B5.

The observed light curves were smoothed with a linear regression using a Gaussian kernel described in Section A. The full set of light-curve fits is shown in Appendix Figures B6—B9. We determined the time of maximum luminosity by a method similar to that used by Gall et al. (2015). We fit a first-order polynomial to a three-day window of our smoothed light curve, and then shifted the window along the light curve. The algorithm was terminated when the slope of the polynomial surpassed -0.01 mag day^{-1}. The termination position of the algorithm was determined as the time of maximum luminosity. The change in magnitude between peak and 15 days post-peak, Δm_{15} (Phillips 1993), was determined by interpolating the smoothed light curve to 15 days after the time of maximum and subtracting the peak magnitude. These values are listed in Table 2.

3.2. Comparison to RW11

Care should be taken when comparing observations in the optical bands with RW11 or other models such as those of Nakar & Sari (2010), which converge at $t \approx 1$ day (note that all times given in this paper, unless stated otherwise, are relative to the estimated date of explosion and are given in the rest frame). The appropriate model has two strong requirements for validity: first, the emitting region must have originated in layers δ_m that were initially close to the surface of the star, $\delta_m \equiv (R_* - r)/R_* \ll 1$; second, the temperature must be greater than 1 eV, where Thomson scattering is dominant and recombination is negligible (see the beginning of Section 3 in RW11). Breakdown of the first assumption causes the dominant divergence of the solution by changing the final velocity of each element (f_ν) from the asymptotic value used, $f_\nu = 2$. This induces an *underestimation* of the temperature (discussed in Section 3.1 of RW11), causing an overestimation of the luminosity, as can be seen in the model overshoot at later times of most

of the fits presented in Appendix Figures B13—B15.

Extending the fit to $t > 4$ days forces the naturally overshooting region to coincide with the peak data. This has two effects: first, the $t < 4$ day data get undershot; second, this procedure effectively shortens the rise time in the model, which reduces the probability of large radii. An example of the RW11 fit, and the effect of extending the fit beyond four days, is shown in Figure 5.

As in González-Gaitán et al. (2015) and Gall et al. (2015), RSG models were compared to the sample without distinguishing between Type II-P and II-L SNe. This is justified for the following two reasons: first, there is evidence that Type II-P and II-L SNe may form a continuum in both their photometric and spectroscopic properties (see Anderson et al. 2014; Gutiérrez et al. 2014, this work), making it unlikely that they originate from different progenitors. Second, blue supergiants are unlikely progenitors primarily because their small radii (Kudritzki et al. 2008) will cause severe adiabatic losses, and they will not have the energy budget to reach the peak luminosity of Type II-L SNe which can peak above -18 (Figure 9). Yellow hypergiants are extremely rare (Oudmaijer et al. 2009), and they are known to be associated with Type IIb SNe (Maund et al. 2011). This leaves RSGs as a reasonable default for the progenitors of Type II-P and II-L SNe.

In order to compare with RW11 models, we selected only those events with at least five detections in the first four days from explosion; this left 33 events. We then generated bolometric light curves using Equation 14 of RW11 (appropriate for RSGs, $n = 3/2$):

$$L = 8.5 \times 10^{42} \frac{E_{51}^{0.92} R_{*,13}}{f_\rho^{0.27} (M/M_\odot)^{0.84} \kappa_{0.34}^{0.92}} t_5^{-0.16} \text{ erg s}^{-1}, \quad (1)$$

where the explosion energy $E_{51} = E/10^{51}$ erg, the progenitor radius $R_{*,13} = R/10^{13}$ cm, the opacity $\kappa_{0.34} = \kappa/0.34$ g^{-1} cm^2, the ejecta mass M, and the time from explosion $t_5 = t/10^5$ s. Also, $f_\rho \equiv \rho_{1/2}/\bar{\rho}$, where $\bar{\rho}$ is the mean density of the ejecta and $\rho_{1/2}$ is the density at $r = R_*/2$. Note that n is the index of the density at the edge of the ejecta given by $\rho(r_0) = \rho_{1/2}\delta^n$. The apparent R-band magnitude was calculated with the photospheric temperature given in Equation 13 of RW11,

$$T_{\rm ph} = 1.6 f_\rho^{-0.037} \frac{E_{51}^{0.027} R_{*,13}^{1/4}}{(M/M_\odot)^{0.054} \kappa_{0.34}^{0.28}} t_5^{-0.45} \text{ eV}, \quad (2)$$

corrected to the color temperature with the factor $T_{\rm c} = 1.2 T_{\rm ph}$ (see discussion in RW11, their Section 3.2 and Figure 1). Then the modeled R-band magnitudes were calculated with the *synphot* routine (Ofek 2014).

We generated light curves for a grid of RSG progenitors with radii $R_* = 10^2$–10^3 R$_\odot$ (200 points logarithmically spaced), explosion energies $E_{51} \equiv E/10^{51}$ erg $= 10^{-2}$–10^2 (250 points logarithmically spaced), a fixed ejected mass $M_{10} \equiv M/(10\ M_\odot) = 1$,[34] $f_\rho = 0.1$, $\kappa_{0.34} = 1$, and various times of explosion within our uncertainty on this

---

[34] The early-time light curve depends on the energy per unit mass; therefore, the possible diversity in M is covered by our range of E_{51}. For further discussion see Rabinak & Waxman (2011) and Ganot et al. (2014).

date (50 points linearly spaced between $t_0 \pm \Delta t_0$).

With the model light curves in hand, we calculated the χ^2 values for the observed flux (in the first 4 days from explosion) for all combinations of the radius, explosion energy per unit mass, and all possible dates of explosion. Finally, we scaled the flux errors until the minimal χ^2 reached 1.[35] The energy per unit mass was estimated at the minimum χ^2 of the grid, and the 95% confidence interval was estimated using a profile likelihood: finding optimal t_0 and R_* for each energy, and then finding values of E_{51} where the cumulative distribution function $\text{CDF}(\chi^2) \leq 0.95$. The E/M values we determined are listed in Table 2, and are shown in Figure 6.

To calculate the mean value of E/M, we have to correct for Malmquist bias. We used an effective distance modulus DM^* such that all SNe would have the same peak apparent magnitude as the faintest SN in our sample with the formula

$$\text{Max}\{m^{\text{peak}}\} = M_i^{\text{peak}} + DM_i^*, \qquad (3)$$

where $\text{Max}\{m^{\text{peak}}\}$ is the faintest peak apparent magnitude in the sample, DM_i^* is the effective distance modulus that sets the peak absolute magnitude M_i^{peak} equal to the faintest peak apparent magnitude. Then the mean SN E/M value in the sample was calculated as

$$\left\langle \frac{E}{M} \right\rangle = \frac{\Sigma_i \, (E/M)_i \, / D_i^{*3}}{\Sigma_j 1/D_j^{*3}}, \qquad (4)$$

where D^* is the luminosity distance taken from the relation

$$DM^* = 5 \log_{10} \left(\frac{D^*}{10 \text{ pc}} \right). \qquad (5)$$

This procedure accounts for the overrepresentation of luminous events in our flux-limited sample. By weighting according to their equivalent volume, less-luminous events — which naturally have a small volume — get put on equal footing with more-luminous events. The corrected histogram of E/M values is shown in Figure 6.

3.3. Spectroscopy

We estimate the expansion velocity of each SN by measuring the minimum of the Hα P-Cygni profile. This was accomplished by fitting a second-order polynomial to the Hα absorption. In order to normalize the velocities to a uniform epoch, the relation from Faran et al. (2014a) was used, relating the velocities measured to the velocity on day 50 for SNe II-P. The relation is given by

$$v_{50} = v_{\text{H}\alpha}(t) \left(\frac{t}{50} \right)^{0.412 \pm 0.02}. \qquad (6)$$

The measured velocities are presented in Table 2.

3.4. ^{56}Ni Mass Estimation

For eight events which had good late-time coverage, we fit for the synthesized radioactive nickel mass. The luminosity per unit mass released by radioactive ^{56}Ni is given by

$$l = 3.9 \times 10^{10} e^{-t/\tau_{\text{Ni}}} + \qquad (7)$$
$$7 \times 10^9 \left(e^{-t/\tau_{\text{Co}}} - e^{-t/\tau_{\text{Ni}}} \right) \text{ erg g}^{-1} \text{ s}^{-1},$$

where τ_{Ni} and τ_{Co} are 8.8, and 111.09 days, respectively. For each of the relevant SNe, we fit the initial nickel mass by minimizing the linear least-squares equation

$$L(t_i) = M_{\text{Ni}} l(t_i), \qquad (8)$$

where $L(t_i)$ and $l(t_i)$ are (respectively) the observed luminosity and expected luminosity per unit mass at time t_i, and M_{Ni} is the initial nickel mass. We also fit three events from the literature for which the authors derived ^{56}Ni masses using multi-band quasi-bolometric light curves (SN 2005cs, SN 2012aw, and SN 2013ab; Figure 8), and found that our values for M_{Ni} are sufficiently close to justify no bolometric correction. However, to be conservative, we assume a 50% uncertainty in our derived ^{56}Ni mass. These values are reported in Table 2.

4. RESULTS

Figure 5 shows an example of the fit to a RW11 model. We found that RW11 models describe the early-time light curves well in most cases (Appendix Figures B13—B15). For each combination of E/M and R_* the time of explosion was selected that minimizes the χ^2. The contours represent the 68%, 95%, and 99.7% χ^2 confidence intervals. Figure 5 is typical, and demonstrates that while the radius of the progenitor cannot be constrained based on the early-time R-band light curve, E/M can be estimated to better than a factor of five.

The energies derived for each SN and the cumulative fraction of events below a given E/M are shown in Figure 6. We find that E/M spans a range of $\sim (0.2-20) \times 10^{51}$ erg/(10 M$_\odot$). Moreover, the E/M values deduced from the fit to RW11 models are significantly (P-value $\ll$ 0.05) correlated with the observed photospheric velocity (Figure 7).[36] Taking the confidence interval as symmetric, a power-law fit gives

$$E_{51}/M_{10} = (2.1 \pm 4.8) \times 10^{-4} \qquad (9)$$
$$\times (v_{50}/10^3 \text{ km s}^{-1})^{4.5 \pm 1.1},$$

where the uncertainties are 95% confidence intervals. We find that E/M from the fit is also significantly correlated with the peak magnitude (Figure 7), and is related to the peak luminosity by

$$E_{51}/M_{10} = (1.71 \pm 0.17) L_{\text{peak}}/10^{42} \text{ erg} \qquad (10)$$
$$- (8.4 \pm 6.2) \times 10^{-2},$$

where L_{peak} is the peak luminosity.

---

[35] The flux errors from our pipeline are underestimated, leading to high χ^2 for models which fit the data well. The errors were scaled to allow for the comparison of different models to each other. The scaling values are presented in Appendix Figures B13—B15.

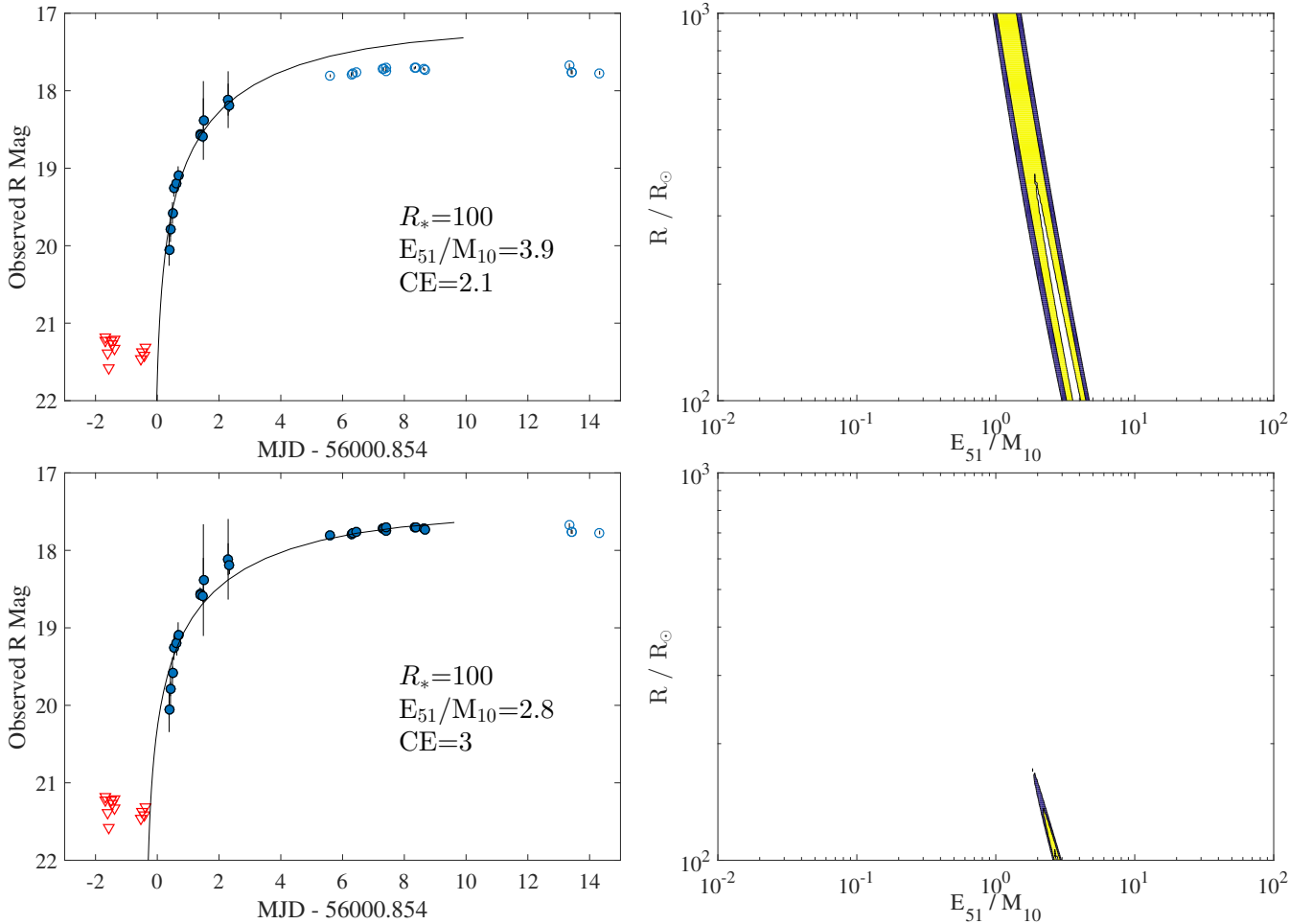[36] All correlations reported were calculated using the Spearman correlation test.

Figure 5. Top left: Example RW11 best fit to PTF12bro. The values of the progenitor radius R, explosion energy per unit mass E_{51}/M_{10}, and error scaling factor CE are displayed. Only filled symbols were included in the fit. Top right: The projection of χ^2 onto the $R - E$ plane (at optimal explosion date t_0 for each point). The contours of 68%, 95%, and 99.7% confidence intervals are shown. Bottom left, right: Best fit to PTF12bro and χ^2 contours including data where $t \leq 10$. Notice that including later data reduces the probability for higher radii.

We added to our sample several events from the literature which have determined parameters from hydrodynamic light-curve modeling (see Table 3). Three SNe (SN 2005cs, SN 2012aw, and SN 2013ab) were sufficiently well sampled during their rise to allow us to perform our RW11 analysis, although it was necessary to slightly relax our criteria and include R-band data up to day 6 from explosion. We found our results to be consistent with the estimated explosion parameters from the literature (Figure 8); however, we derive a higher E/M value for SN 2013ab than do Bose et al. (2015). Bose et al. (2015) estimated E/M from hydrodynamic modeling, making it difficult to assess the source of this discrepancy. Note that our derived ^{56}Ni mass of $\sim 5 \times 10^{-3}$ M$_\odot$ for iPTF13aaz (SN 2013am) is lower than the 1.5×10^{-2} M$_\odot$ reported by Zhang et al. (2014), but the source of this discrepancy is unclear. We find that the ^{56}Ni mass is strongly correlated with E/M ($\rho = 0.76$, P-value $<< 0.05$; Figure 8). This result has been observed in Type Ib/c SNe (Mazzali et al. 2013), and is in line with models such as that of Kushnir (2015), which predict that more ^{56}Ni is produced by more-energetic SN II explosions.

In addition, we find several empirical correlations (Figure 9). The peak luminosity is significantly and strongly correlated with Δm_{15} — brighter events decline faster. This is the opposite of well-established trends in SNe Ia and Ib/c (Phillips 1993) that are powered by ^{56}Ni during their rise, and is in agreement with the findings of Anderson et al. (2014) for Type II V-band light curves. The peak luminosity is also correlated with v_{50}: brighter events have higher velocities at day 50. This relation has already been established for Type II-P SNe (Hamuy & Pinto 2002; Nugent et al. 2006), although it has not been demonstrated until now for SNe II generally. The rise time is more weakly correlated with Δm_{15}, and with a larger scatter, although it significantly shows that slower risers are also faster decliners. We do not observe a significant correlation between the rise time and the peak luminosity, contrary to the suggestions of Gal-Yam et al. (2011) and Gall et al. (2015).

5. DISCUSSION

We have performed the first direct fitting of analytical early light-curve models (RW11) to a large sample of Type II SNe with a well-sampled rise. Our results
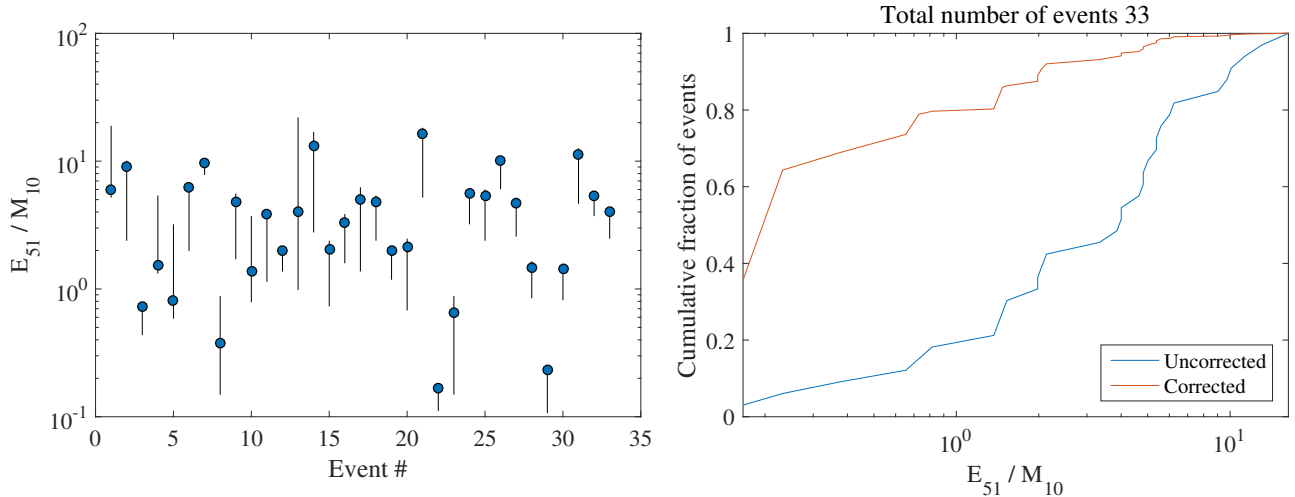
Figure 6. Left: E/M derived from RW11 with 95% profile likelihood confidence intervals. Right: Cumulative fraction of events below a given E/M, corrected and uncorrected for Malmquist bias.
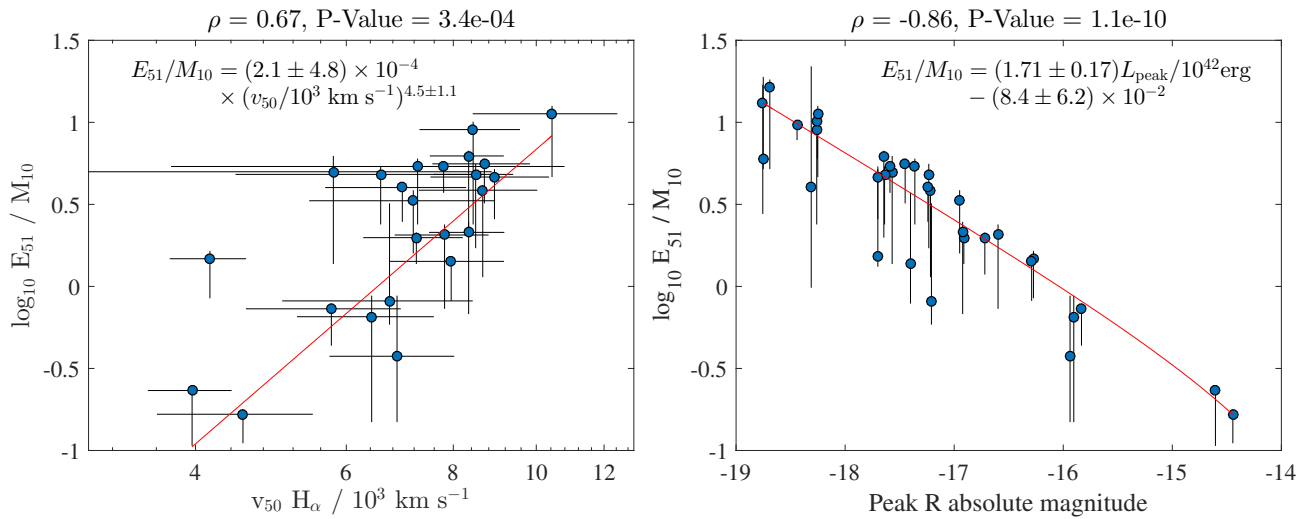

Figure 7. Left: E/M from the fit to RW11 as a function of the velocity normalized to v_{50} of Hα. Right: E/M from RW11 as a function of peak magnitude. Red lines are the best fits described in the text.

show that, assuming a RSG progenitor, we can deduce the value of E/M to within roughly a factor of five from early-time optical light curves. Progenitor radii are not constrained by R-band data alone, and require UV observations (Ganot et al. 2014).

Gall et al. (2015) and González-Gaitán et al. (2015) recently compared light curves to RW11/NS10 shock-cooling models and found that only small radii ($R < 400$ R$_\odot$) appeared to be consistent with observations, in strong tension with direct measurements of Type II-P SNe (Smartt et al. 2009; Smartt 2015). However, Valenti et al. (2014) and Bose et al. (2015) compared single objects and found no such discrepancy.

It appears that the Gall et al. (2015) and González-Gaitán et al. (2015) method of extracting a rise time from the models and comparing it to the rise time of their light curves is inaccurate. The models are valid for a brief ($t \approx 4$ days) period before important assumptions such as the emission coming from a thin shell at the edge of the star, and the temperature being well above 1 eV,

begin to break down. As was explained in Section 3, the breakdown of these assumptions leads to an overshoot of the data at later times ($t > 4$ days). By comparing to rise times from the models, these works rejected models which fit the early photometric data well.

Figure 10 demonstrates this using LSQ13cuw, a well-sampled event from Gall et al. (2015). We fit two extreme cases, with radii of 100 and 1000 R$_\odot$, to the first six days of data. Both models fit the early-time data equally well. While the 100 R$_\odot$ model has a consistent rise time with LSQ13cuw, it does not agree at all with the photometry near peak. We suspect that this explains the apparent discrepancy between the radii inferred from the models by Gall et al. (2015) and González-Gaitán et al. (2015), and the measured RSG radii (Smartt et al. 2009) of the progenitors of SNe II-P.

We find a strong correlation between the RW11 E/M values and the SN expansion velocity at day 50. Because v_{50} is an independent estimate of E/M, this provides support for the deduced E/M values. We find that our
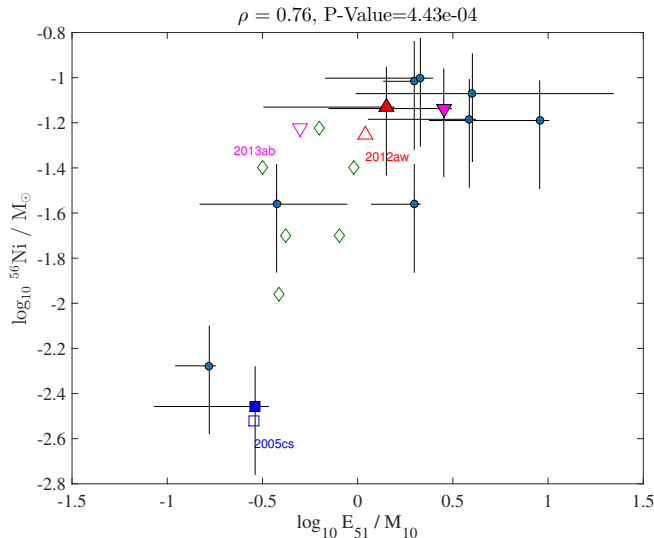
Figure 8. E/M from the fit to RW11 vs. ^{56}Ni mass. Empty symbols are taken from the literature (Table 3) with parameters estimated from hydrodynamic modeling. The blue, red, and magenta filled (empty) symbols represent our (literature) estimates of the parameters of SN 2005cs, SN 2012aw, and SN 2013ab. Note the good agreement in ^{56}Ni mass between our analysis and the literature. The source of the discrepancy between our E/M estimate for SN 2013ab and that of Bose et al. (2015) is unclear, due to the different methods used. Diamonds represent events from the literature which did not have sufficient early-time data on which to perform our analysis.

sample has a mean energy per unit mass, corrected for Malmquist bias, of $\langle E_{51}/M_{10} \rangle = 0.85$, with a range of $E_{51}/M_{10} \approx 0.2$–20. Because the progenitor mass of a SN II-P is suggested to be confined to a relatively narrow range (8–16 $M_{\odot}$; Smartt et al. 2009), our results lead to the conclusion that there is a significant intrinsic diversity in explosion energies. The correlation between peak magnitude and E/M indicates that more energetic explosions also have higher peak luminosity. In addition, the strong positive correlation between E/M and ^{56}Ni mass implies that stronger explosions produce more ^{56}Ni. This result is consistent with the predictions of some models, including those of Kushnir & Katz (2015) and Kushnir (2015), claiming that the explosion mechanism of CC SNe is thermonuclear detonation of the infalling outer shells.

In our sample, we do not find that the rise time and peak magnitude of SNe II are correlated (Figure 9). Although it was suggested in the past that brighter SNe II-P may have longer rise times (Gal-Yam et al. 2011), our sample of well-monitored light curves disfavors this hypothesis. Our correlation between Δm_{15} and the peak magnitude recovers a relation previously shown by Anderson et al. (2014) in the V band. We also find, however, that Δm_{15} is correlated with the rise time, although with a large scatter. SNe with longer rise times also decline faster.

Nicholl et al. (2015) have recently explored various mechanisms to explain hydrogen-poor superluminous SNe (SLSNe, Gal-Yam 2012). Their models include magnetars (Kasen & Bildsten 2010; Woosley 2010), circumstellar interaction (Woosley et al. 2007; Ofek et al. 2010; Chevalier & Irwin 2011), and ^{56}Ni radioactive decay. They find an opposing correlation to ours: in hydrogen-poor SLSNe, as well as in all of the above-mentioned

models, longer-rising SNe also decline more slowly. We interpret this as evidence that Type II SNe are not powered by any of these potential sources during their early phase.

6. SUMMARY

Our main conclusions regarding SNe II can be summarized as follows.

- The progenitor radius cannot be inferred by comparison to shock-cooling models based on R-band photometry alone. The value of E/M can be inferred to within a factor of five.

- The mean SN II energy per unit mass, corrected for Malmquist bias, is $\langle E/M \rangle = 0.85 \times 10^{51}$ erg/(10 $M_{\odot}$), and has a range of (0.2–20) $\times 10^{51}$ erg/(10 $M_{\odot}$).

- The derived value of E/M from RW11 models is strongly correlated with the photospheric velocity at day 50, peak magnitude, and ^{56}Ni mass produced in the explosion.

- Δm_{15} is correlated with the rise time — slower risers are also faster decliners. This indicates that Type II SNe are unlikely to be powered by radioactive decay or other central-engine models at early times.

While it was not possible to infer the radius from R-band data alone, the path for future work is clear. Multiband light curves, which will be acquired by future surveys such as the Zwicky Transient Facility (ZTF; Bellm 2014; Smith et al. 2014) and the Large Synoptic Survey Telescope (LSST; Ivezic et al. 2008), as well as early-time UV photometry from satellites such as ULTRASAT (Sagiv et al. 2014), will drastically reduce the uncertainties in determining the progenitor radius. The benefit will be twofold: these facilities will reduce uncertainties in the time of first light, and there will be more useful photometry within the window of validity of available shock-cooling models, because the rise time is much shorter in blue and UV bands.
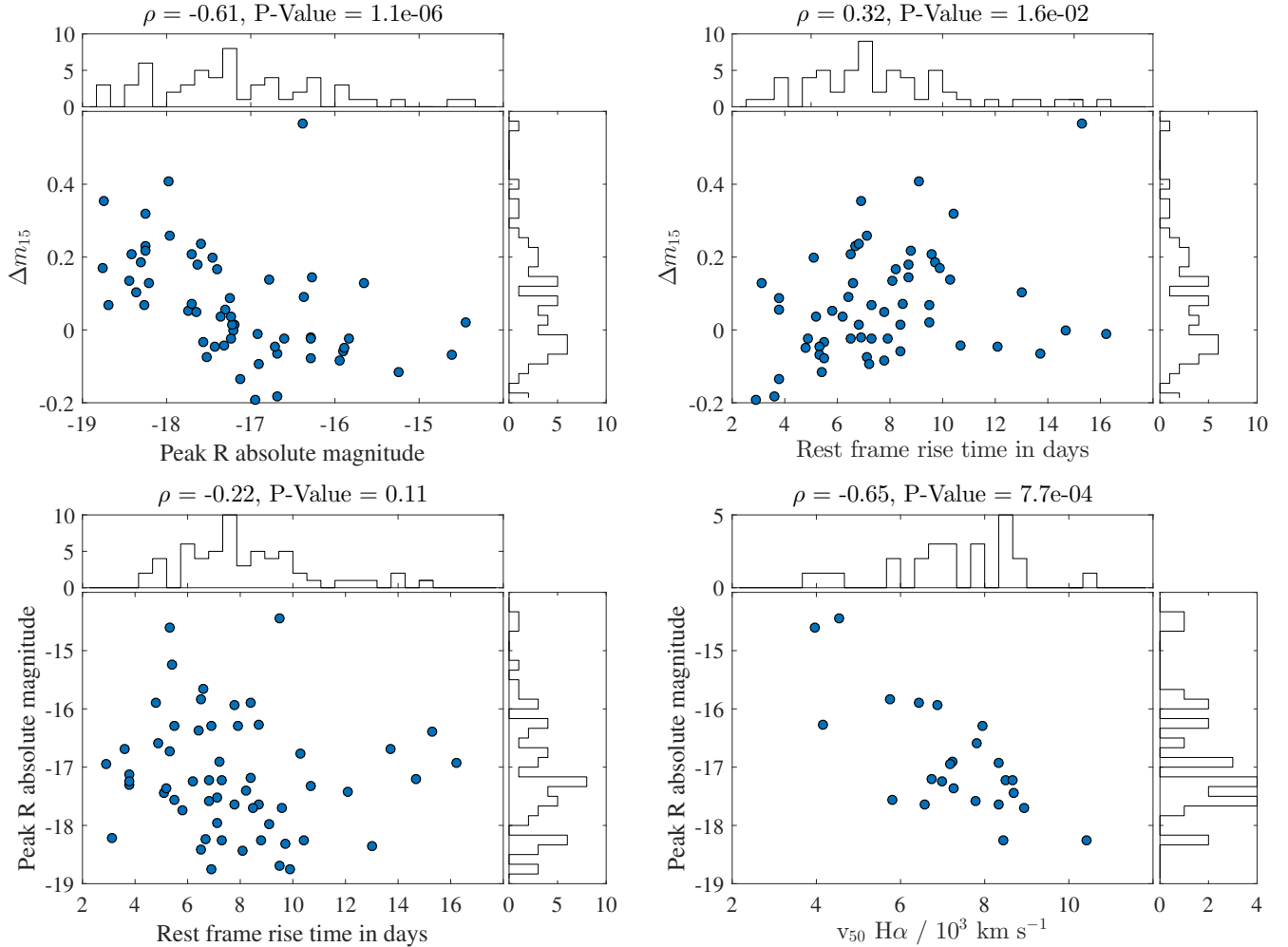
Figure 9. Top left: Δm_{15} as a function of the peak magnitude. Top right: Δm_{15} as a function of rise time. Bottom left: Peak magnitude as a function of rise time, derived from the smoothed light curves (Appendix Figures B6—B9). Bottom right: Peak magnitude as a function of v_{50}.

REFERENCES

Anderson, J. P., González-Gaitán, S., Hamuy, M., et al. 2014, ApJ, 786, 67

Arcavi, I., Gal-Yam, A., Cenko, S. B., et al. 2012, ApJ, 756, L30

Arcavi, I., Gal-Yam, A., Sullivan, M., et al. 2014, ApJ, 793, 38

Barbarino, C., Dall'Ora, M., Botticella, M. T., et al. 2015, MNRAS, 448, 2312

Bellm, E. 2014, eprint: arXiv:1410.8185, 27–33

Blondin, S., & Tonry, J. L. 2007, ApJ, 666, 1024

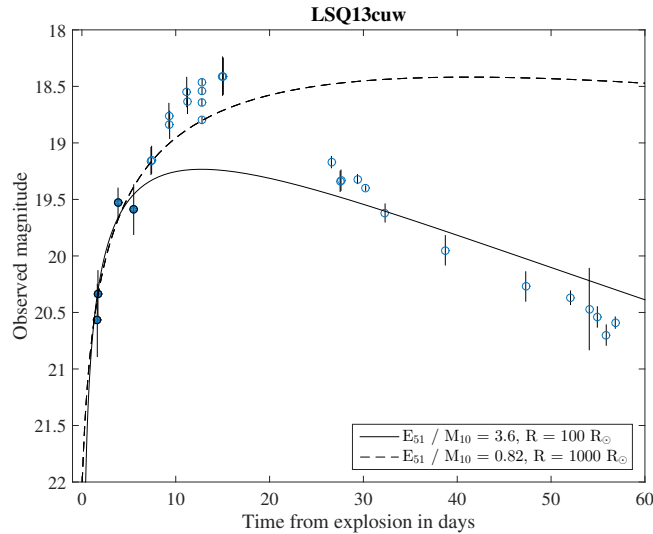Bose, S., Valenti, S., Misra, K., et al. 2015, MNRAS, 450, 2373

Figure 10. Comparison of RW11 models to LSQ13cuw photometry from Gall et al. (2015). Note that while they differ greatly in rise time, models with progenitor radii of 100–1000 $R_\odot$ are consistent with the early-time measurements. Data up to day 6 were included in the fit (filled symbols).

Brown, T. M., Baliber, N., Bianco, F. B., et al. 2013, PASP, 125, 1031

Cenko, S. B., Fox, D. B., Moon, D.-S., et al. 2006, PASP, 118, 1396

Chevalier, R. A., & Irwin, C. M. 2011, ApJL, 729, L6

Dall'Ora, M., Botticella, M. T., Pumo, M. L., et al. 2014, ApJ, 787, 139

Faber, S. M., Phillips, A. C., Kibrick, R. I., et al. 2003, in Proc. of SPIE, Vol. 4841, 1657–1669

Faran, T., Poznanski, D., Filippenko, A. V., et al. 2014a, MNRAS, 442, 844

—. 2014b, MNRAS, 445, 554

Filippenko, A. V. 1997, ARA&A, 35, 309

Firth, R. E., Sullivan, M., Gal-Yam, A., et al. 2015, MNRAS, 446, 3895

Gal-Yam, A. 2012, Science, 337, 927

Gal-Yam, A., Kasliwal, M. M., Arcavi, I., et al. 2011, ApJ, 736, 159

Gal-Yam, A., Arcavi, I., Ofek, E. O., et al. 2014, Nature, 509, 471

Gall, E. E. E., Polshaw, J., Kotak, R., et al. 2015, A&A, 582, A3

Ganot, N., Gal-Yam, A., Ofek, E. O., et al. 2014, arXiv:1412.4063 [astro-ph]

Gezari, S., Dessart, L., Basa, S., et al. 2008, ApJL, 683, L131

González-Gaitán, S., Tominaga, N., Molina, J., et al. 2015, MNRAS, 451, 2212

Gutiérrez, C. P., Anderson, J. P., Hamuy, M., et al. 2014, ApJ, 786, L15

Hamuy, M., & Pinto, P. A. 2002, ApJL, 566, L63

Inserra, C., Baron, E., & Turatto, M. 2012, MNRAS, 422, 1178

Ivezic, Z., Tyson, J. A., Abel, B., et al. 2008, arXiv:0805.2366 [astro-ph], arXiv: 0805.2366

Kasen, D., & Bildsten, L. 2010, ApJ, 717, 245

Kiewe, M., Gal-Yam, A., Arcavi, I., et al. 2012, ApJ, 744, 10

Kinney, A. L., Calzetti, D., Bohlin, R. C., et al. 1996, ApJ, 467, 38

Kudritzki, R.-P., Urbaneja, M. A., Bresolin, F., et al. 2008, ApJ, 681, 269

Kulkarni, S. R. 2013, ATel, 4807, 1

Kushnir, D. 2015, arXiv:1502.03111 [astro-ph], arXiv: 1502.03111

Kushnir, D., & Katz, B. 2015, ApJ, 811, 97

Law, N. M., Kulkarni, S. R., Dekany, R. G., et al. 2009, PASP, 121, 1395

Maguire, K., Di Carlo, E., Smartt, S. J., et al. 2010, MNRAS, 404, 981

Matheson, T., Filippenko, A. V., Ho, L. C., Barth, A. J., & Leonard, D. C. 2000, AJ, 120, 1499

Maund, J. R., Fraser, M., Ergon, M., et al. 2011, ApJ, 739, L37

Mazzali, P. A., Walker, E. S., Pian, E., et al. 2013, MNRAS, 432, 2463

Miller, J. S., & Stone, R. P. S. 1993, Lick Obs. Tech. Rep., 66

Munari, U., Henden, A., Belligoli, R., et al. 2013, NewA, 20, 30

Nakar, E., & Sari, R. 2010, ApJ, 725, 904

Nicholl, M., Smartt, S. J., Jerkstrand, A., et al. 2015, MNRAS, 452, 3869

Nugent, P., Sullivan, M., Ellis, R., et al. 2006, ApJ, 645, 841

Ofek, E. O. 2014, Astrophysics Source Code Library, 1407.005

Ofek, E. O., Rabinak, I., Neill, J. D., et al. 2010, ApJ, 724, 1396

Ofek, E. O., Arcavi, I., Tal, D., et al. 2014, ApJ, 788, 154

Oke, J. B., & Gunn, J. E. 1982, PASP, 94, 586

Oke, J. B., Cohen, J. G., Carr, M., et al. 1995, PASP, 107, 375

Oudmaijer, R. D., Davies, B., de Wit, W.-J., & Patel, M. 2009, in ASP Conf. Ser., Vol. 412, 17

Pastorello, A., Valenti, S., Zampieri, L., et al. 2009, MNRAS, 394, 2266

Pastorello, A., Pumo, M. L., Navasardyan, H., et al. 2012, A&A, 537, A141

Phillips, M. M. 1993, ApJL, 413, L105

Rabinak, I., & Waxman, E. 2011, ApJ, 728, 63

Rau, A., Kulkarni, S. R., Law, N. M., et al. 2009, PASP, 121, 1334

Sagiv, I., Gal-Yam, A., Ofek, E. O., et al. 2014, AJ, 147, 79

Sanders, N. E., Soderberg, A. M., Gezari, S., et al. 2015, ApJ, 799, 208

Schawinski, K., Justham, S., Wolf, C., et al. 2008, Science, 321, 223

Schlegel, D. J., Finkbeiner, D. P., & Davis, M. 1998, ApJ, 500, 525

Schlegel, E. M. 1990, MNRAS, 244, 269

Silverman, J. M., Foley, R. J., Filippenko, A. V., et al. 2012, Monthly Notices of the Royal Astronomical Society, 425, 1789

Smartt, S. J. 2015, PASA, 32, e016

Smartt, S. J., Eldridge, J. J., Crockett, R. M., & Maund, J. R. 2009, MNRAS, 395, 1409

Smith, N., Mauerhan, J. C., Cenko, S. B., et al. 2015, MNRAS, 449, 1876

Smith, R. M., Dekany, R. G., Bebek, C., et al. 2014, in Proc. of SPIE, Vol. 9147, 914779

Soderberg, A. M., Berger, E., Page, K. L., et al. 2008, Nature, 453, 469

Sullivan, M., Howell, D. A., Perrett, K., et al. 2006, AJ, 131, 960

Takáts, K., Pumo, M. L., Elias-Rosa, N., et al. 2014, MNRAS, 438, 368

Tomasella, L., Cappellaro, E., Fraser, M., et al. 2013, MNRAS, 434, 1636

Valenti, S., Sand, D., Pastorello, A., et al. 2014, MNRAS, 438, L101

Woosley, S. E. 2010, ApJL, 719, L204

Woosley, S. E., Blinnikov, S., & Heger, A. 2007, Nature, 450, 390

Yaron, O., & Gal-Yam, A. 2012, PASP, 124, 668

Zhang, J., Wang, X., Mazzali, P. A., et al. 2014, ApJ, 797, 5

Table 1
List of supernovae included in this study.

PTF name	α(J2000)	δ(J2000)	z	DM[a]	A_R[b]	A_r[b]	Classification spectrum UT Date	Instrument
09cjq[c]	21:16:28.483	−00:49:39.71	0.02	34.69	0.16	0.17	2009-10-22	Keck-1 — LRIS
09ecm	01:06:43.164	−06:22:40.89	0.0285	35.47	0.34	0.36	2009-10-22	Keck-1 — LRIS
09fma	03:10:23.327	−09:59:58.04	0.031	35.66	0.23	0.25	2010-01-09	P200 — DBSP
10abyy	05:16:40.524	+06:47:53.76	0.0297	35.56	0.37	0.39	2011-01-13	Lick-3m — Kast
10bgl[d]	10:19:04.697	+46:27:23.34	0.03	35.58	0.03	0.03	2010-02-06	Keck-1 — LRIS
10gva	12:23:55.397	+10:34:50.62	0.025	35.18	0.08	0.08	2010-06-12	Keck-1 — LRIS
10gxi	12:44:33.681	+31:05:05.35	0.0287	35.48	0.04	0.04	2010-07-19	P200 — DBSP
10jwr	16:12:15.986	+32:04:14.49	0.059	37.10	0.06	0.06	2010-07-07	Keck-1 — LRIS
10mug	15:04:06.828	+28:29:17.84	0.06	37.14	0.07	0.08	2010-08-14	P200 — DBSP
10osr	23:45:45.161	+11:28:42.37	0.0235	35.04	0.11	0.12	2010-10-11	Lick-3m — Kast
10pjg	23:23:08.010	+13:02:39.18	0.0384	36.13	0.14	0.15	2010-09-06	P200 — DBSP
10qwz	23:35:18.607	+12:55:31.81	0.02	34.69	0.16	0.17	2010-10-11	Lick-3m — Kast
10rem	17:17:43.596	+20:52:30.91	0.046	36.54	0.15	0.16	2010-10-12	Keck-2 — DEIMOS
10uls	01:21:22.659	+04:53:28.75	0.044	36.44	0.08	0.09	2010-10-11	Mayall — RC Spec
10umz	01:22:01.640	−01:57:23.30	0.052	36.81	0.11	0.12	2010-10-30	WHT-4.2m — ISIS
10uqg	17:17:00.337	+27:29:27.48	0.048	36.63	0.12	0.13	2010-10-03	Keck-1 — LRIS
10uqn[e]	23:06:57.458	+03:56:24.21	0.0482	36.64	0.14	0.15	2010-10-03	Keck-1 — LRIS
10vdl	23:05:48.879	+03:31:25.54	0.016	34.19	0.15	0.17	2010-11-07	Keck-2 — DEIMOS
10xtq	08:23:14.292	+21:57:58.00	0.08	37.79	0.11	0.12	2010-12-06	P200 — DBSP
11ajz	08:26:49.200	+20:22:32.29	0.025	35.18	0.08	0.09	2011-03-10	P200 — DBSP
11cwi	16:52:28.515	+21:42:00.99	0.056	36.98	0.15	0.16	2011-05-13	Mayall — RC Spec
11go	11:32:00.235	+53:42:38.06	0.0268	35.33	0.03	0.03	2011-03-10	P200 — DBSP
11hsj	16:57:58.151	+55:11:01.14	0.0287	35.48	0.05	0.05	2011-09-29	Lick-3m — Kast
11htj	21:16:03.503	+12:31:20.95	0.017	34.33	0.18	0.19	2011-10-30	P200 — DBSP
11iqb	00:34:04.836	−09:42:17.92	0.0125	33.65	0.08	0.09	2011-08-28	P200 — DBSP
11izt	01:52:25.944	+35:30:21.80	0.02	34.69	0.14	0.15	2011-08-31	WHT-4.2m — ISIS
11qax	23:42:25.584	+00:15:16.83	0.022	34.90	0.06	0.07	2011-12-18	Lick-3m — Kast
12bbm	11:01:51.229	+45:28:49.60	0.0446	36.47	0.03	0.04	2012-03-23	Keck-1 — LRIS
12bro	12:24:17.054	+18:55:27.96	0.0227	34.96	0.09	0.10	2012-04-29	P200 — DBSP
12bvh	10:43:53.752	+11:40:17.89	0.0026	30.22	0.07	0.07	2012-05-21	Lick-3m — Kast
12cod	13:22:35.288	+54:48:47.11	0.0118	33.52	0.08	0.08	2012-05-31	TNG — DOLORES
12efk	16:24:43.887	+31:51:37.14	0.0931	38.14	0.05	0.06	2012-06-16	Keck-1 — LRIS
12fip	15:00:51.041	+09:20:25.12	0.034	35.86	0.07	0.08	2012-07-21	P200 — DBSP
12fo	12:58:36.924	+27:10:24.94	0.026	35.26	0.04	0.04	2012-01-27	Mayall — RC Spec
12ftc	15:05:01.880	+20:05:54.63	0.0732	37.59	0.09	0.10	2012-07-27	P200 — DBSP
12gnn	15:58:49.278	+36:10:10.95	0.0308	35.64	0.06	0.07	2012-08-21	WHT-4.2m — ISIS
12grj	01:20:39.003	+04:46:23.77	0.034	35.86	0.07	0.08	2012-07-19	P200 — DBSP
12hsx	00:55:03.328	+42:19:52.01	0.019	34.57	0.23	0.25	2012-08-19	Keck-1 — LRIS
12krf	22:48:16.673	+24:08:58.25	0.0625	37.23	0.37	0.40	2012-12-05	P200 — DBSP
13aaz	11:18:56.939	+13:03:50.03	0.00269	30.30	0.06	0.07	2013-05-02	P200 — DBSP
13kg[e]	11:34:36.446	+54:53:23.69	0.019	34.57	0.04	0.04	2013-06-06	Keck-2 — DEIMOS
13bjx	14:14:52.106	+36:47:28.58	0.0279	35.42	0.02	0.02	2013-08-03	P200 — DBSP
13bld[e]	16:24:54.586	+41:02:59.24	0.0331	35.80	0.02	0.02	2013-07-05	P200 — DBSP
13bsg	13:50:07.229	+33:45:07.46	0.061	37.17	0.06	0.07	2013-07-05	P200 — DBSP
13ccu	02:08:51.874	+41:49:32.80	0.074	37.61	0.19	0.21	2013-08-14	P200 — DBSP
13clj	01:30:40.412	+14:28:50.04	0.056	36.98	0.11	0.12	2013-09-04	P200 — DBSP
13cly	00:12:46.944	+04:40:34.59	0.0428	36.37	0.06	0.06	2013-09-03	Magellan-Baade — IMACS
13cnk	02:02:12.776	+07:58:38.61	0.04	36.22	0.16	0.17	2013-10-04	Keck-2 — DEIMOS
13dkk	23:41:35.156	+03:43:30.37	0.0092	32.98	0.14	0.15	2013-10-05	P200 — DBSP
13dkz	01:36:11.577	+33:37:01.43	0.016	34.19	0.11	0.12	2013-11-02	P200 — DBSP
13dla	01:02:49.095	−00:44:30.80	0.0518	36.80	0.08	0.09	2013-11-02	P200 — DBSP
13dqy	23:19:44.700	+10:11:04.40	0.0119	33.54	0.10	0.11	2013-11-26	P200 — DBSP
13dzb	03:10:50.199	−00:21:40.32	0.037	36.05	0.18	0.19	2013-11-27	LCOGT — FLOYDS
14abc	12:22:57.328	+28:29:54.75	0.0254	35.21	0.06	0.06	2014-04-04	P200 — DBSP
14adz	13:49:57.814	+37:45:08.49	0.078	37.73	0.03	0.03	2014-04-29	Keck-1 — LRIS
14ajq[d]	12:06:32.001	+39:14:13.65	0.036	35.99	0.08	0.08	2014-04-09	APO 3.5m — DIS
14aoi	12:09:11.543	+29:10:20.90	0.012	33.56	0.05	0.05	2014-06-30	Lick-3m — Kast

[a] Derived using the *lum_dist* routine in MATLAB with the cosmological parameters given in Section 3.
[b] Derived using the *sky_ebv* routine in MATLAB, using $R_V = 3.08$.
[c] The spectrum of this SN has a reddened continuum and Na D absorption lines; it likely suffers from host-galaxy extinction.
[d] The spectrum of this SN has a reddened continuum, but no Na D absorption lines; it may suffer from host-galaxy extinction.
[e] The spectrum of this SN has a blue continuum, but also Na D absorption lines; it could possibly suffer from host-galaxy extinction.

Table 2
List of derived quantities.

PTF name	t_0 MJD	$t_{\rm rise}$ days	Peak R Mag	Δm_{15}	E_{51}/M_{10}	v Hα 10^3 km s^{-1}	Phase days	v_{50} Hα[a] 10^3 km s^{-1}	$M_{\rm Ni}$ M$_\odot$
09cjq	55043.30 ± 2.96	6.9	-16.29	-0.019	—	—	—	—	—
09ecm	55083.94 ± 0.36[b]	12.1	-17.42	-0.045	—	—	—	—	—
09fma	55108.43 ± 1.08	5.8	-17.74	0.054	—	—	—	—	—
10abyy	55536.29 ± 0.90	6.9	-18.75	0.35	$6^{+13}_{-0.83}$	—	—	—	—
10bgl	55197.62 ± 1.00[b]	10.3	-16.77	0.14	—	—	—	—	—
10gva	55320.28 ± 0.90	7.3	-18.26	0.067	$9^{+1.1}_{-6.6}$	9.47 ± 1.1	38	8.44 ± 1.1	0.065 ± 0.032
10gxi	55320.87 ± 2.48	8.4	-17.19	0.013	—	—	—	—	—
10jwr	55354.74 ± 2.49	3.1	-18.21	0.13	—	—	—	—	—
10mug	55373.81 ± 2.49	6.7	-18.24	0.23	—	—	—	—	—
10osr	55389.39 ± 0.93	10.7	-17.31	-0.044	—	—	—	—	—
10pjg	55385.91 ± 2.48	7.9	-16.29	-0.022	—	—	—	—	—
10qwz	55415.87 ± 1.50	6.5	-15.83	-0.024	$0.73^{+0.056}_{-0.3}$	5.24 ± 0.99	63	5.76 ± 1.2	—
10rem	55415.21 ± 1.96	3.6	-16.68	-0.18	—	—	—	—	—
10uls	55445.96 ± 0.48	9.6	-17.70	0.21	$1.5^{+3.9}_{-0.21}$	—	—	—	—
10umz	55444.44 ± 0.61[b]	14.7	-17.21	-0.0021	$0.82^{+2.4}_{-0.23}$	6.64 ± 1.6	52	6.74 ± 1.7	—
10uqg	55448.65 ± 1.50	9.1	-17.97	0.41	—	—	—	—	—
10uqn	55445.36 ± 1.88	3.8	-17.30	0.055	—	—	—	—	—
10vdl	55452.29 ± 1.98	5.4	-15.24	-0.12	—	—	—	—	—
10xtq	55465.99 ± 0.49	6.5	-18.42	0.21	—	—	—	—	—
11ajz	55592.40 ± 0.96	7.8	-17.65	0.049	$6.2^{+0.48}_{-4.3}$	9.47 ± 0.65	37	8.34 ± 0.83	—
11cwi	55672.98 ± 1.48	3.8	-17.13	-0.13	—	—	—	—	—
11go	55570.91 ± 1.41	6.4	-16.37	0.089	—	—	—	—	—
11hsj	55753.38 ± 1.95	7.1	-17.52	-0.076	—	—	—	—	—
11htj	55751.92 ± 1.48	13.7	-16.68	-0.064	—	—	—	—	—
11iqb	55764.68 ± 0.21[b]	8.1	-18.44	0.14	$9.7^{+0.37}_{-1.9}$	—	—	—	—
11izt	55765.91 ± 2.46	7.8	-15.94	-0.083	$0.38^{+0.5}_{-0.23}$	7.76 ± 1.2	37	6.88 ± 1.1	0.027 ± 0.014
11qax	55866.69 ± 0.41	7.3	-17.23	-0.023	$4.8^{+0.77}_{-3.1}$	8.85 ± 0.65	45	8.50 ± 0.9	—
12bbm	55980.38 ± 0.98	8.2	-17.40	0.17	$1.4^{+2.3}_{-0.58}$	—	—	—	—
12bro	56000.85 ± 0.38	6.8	-17.22	0.015	$3.9^{+0.3}_{-2.7}$	9.12 ± 1.3	44	8.66 ± 1.4	0.065 ± 0.033
12bvh	56002.23 ± 0.95	7.2	-16.91	-0.095	$2^{+0.15}_{-0.61}$	6.48 ± 0.67	66	7.24 ± 0.96	0.096 ± 0.048
12cod	56019.41 ± 1.90	9.7	-18.31	0.18	4^{+18}_{-3}	—	—	—	0.085 ± 0.042
12efk	56057.25 ± 0.71[b]	9.9	-18.76	0.17	$13^{+3.9}_{-10}$	—	—	—	—
12fip	56089.23 ± 0.97	4.9	-16.60	-0.023	$2.1^{+0.33}_{-1.3}$	8.71 ± 0.89	38	7.81 ± 0.98	—
12fo	55927.40 ± 0.98	2.9	-16.95	-0.19	$3.3^{+0.53}_{-1.7}$	9.57 ± 2.3	25	7.18 ± 1.8	—
12ftc	56090.35 ± 0.97	5.5	-17.57	-0.032	$5^{+1.2}_{-3.6}$	7.11 ± 3.7	30	5.79 ± 3.1	—
12gnn	56116.39 ± 0.97	8.7	-17.64	0.18	$4.8^{+0.57}_{-2.4}$	7.05 ± 2.2	42	6.58 ± 2.1	—
12grj	56123.45 ± 0.97	5.3	-16.72	-0.045	$2^{+0.15}_{-0.8}$	—	—	—	0.027 ± 0.014
12hsx	56112.92 ± 0.25[b]	16.2	-16.92	-0.01	$2.1^{+0.34}_{-1.5}$	8.77 ± 0.58	44	8.34 ± 0.84	0.099 ± 0.05
12krf	56234.14 ± 0.99	9.5	-18.69	0.069	$16^{+1.9}_{-11}$	—	—	—	—
13aaz	56371.75 ± 1.42	9.5	-14.44	0.021	$0.17^{+0.013}_{-0.056}$	4.88 ± 0.94	42	4.54 ± 0.94	0.0053 ± 0.0026
13akg	56389.70 ± 2.47	8.4	-15.90	-0.06	$0.65^{+0.23}_{-0.5}$	6.03 ± 0.98	58	6.42 ± 1.2	—
13bjx	56442.70 ± 0.48	5.1	-17.45	0.2	$5.6^{+0.43}_{-2.4}$	7.93 ± 0.8	63	8.70 ± 1.1	—
13bld	56442.93 ± 0.46	4.8	-15.89	-0.051	—	—	—	—	—
13bsg	56451.74 ± 0.47	5.2	-17.36	0.037	$5.4^{+0.63}_{-3}$	9.71 ± 4.7	25	7.27 ± 3.5	—
13ccu	56499.38 ± 0.98	7.1	-17.96	0.26	—	—	—	—	—
13clj	56507.90 ± 0.45	10.4	-18.26	0.32	$10^{+0.77}_{-4.1}$	—	—	—	—
13cly	56505.84 ± 0.15[b]	8.5	-17.70	0.073	$4.6^{+0.54}_{-2.1}$	8.20 ± 1.1	62	8.94 ± 1.4	—
13cnk	56509.90 ± 0.46	8.7	-16.27	0.14	$1.5^{+0.17}_{-0.63}$	3.94 ± 0.25	57	4.16 ± 0.43	—
13dkk	56546.84 ± 0.35	5.3	-14.60	-0.069	$0.23^{+0.018}_{-0.13}$	5.46 ± 0.51	23	3.96 ± 0.44	—
13dkz	56547.93 ± 0.45	5.5	-16.29	-0.077	$1.4^{+0.11}_{-0.61}$	8.00 ± 1.1	49	7.95 ± 1.2	—
13dla	56548.95 ± 0.45	8.8	-18.25	0.22	$11^{+1.3}_{-6.6}$	10.74 ± 1.9	47	10.43 ± 2	—
13dqy	56570.79 ± 0.45	6.8	-17.59	0.24	$5.4^{+0.41}_{-1.7}$	7.76 ± 0.44	51	7.79 ± 0.75	—
13dzb	56602.81 ± 0.45	6.2	-17.24	0.038	$4^{+0.31}_{-1.5}$	10.29 ± 1.8	19	6.98 ± 1.3	—
14abc	56732.28 ± 2.92	3.8	-17.25	0.086	—	—	—	—	—
14adz	56735.34 ± 0.36[b]	13.0	-18.36	0.1	—	—	—	—	—
14ajq	56743.40 ± 1.99	15.3	-16.39	0.57	—	—	—	—	—
14aoi	56769.14 ± 0.05[b]	6.6	-15.66	0.13	—	—	—	—	—

[a] Estimated using the relation from Faran et al. (2014a); see Section 3.
[b] From exponential fit.

Table 3
Explosion parameters from events in the literature.

SN	E_{51}/M_{10}	^{56}Ni/M$_\odot$	E_{51}/M_{10}[a]	^{56}Ni/M$_\odot$[a]	Reference
SN 2004et	0.63	0.06	—	—	Maguire et al. (2010)
SN 2005cs	0.29	0.003	$0.29^{+0.05}_{-0.2}$	0.0034 ± 0.0017	Pastorello et al. (2009)
SN 2007od	0.8	0.02	—	—	Inserra et al. (2012)
SN 2009E	0.32	0.04	—	—	Pastorello et al. (2012)
SN 2009N	0.42	0.02	—	—	Takáts et al. (2014)
SN 2012A	0.38	0.011	—	—	Tomasella et al. (2013)
SN 2012aw	1.1	0.056	$1.41^{+0.13}_{-1.09}$	0.074 ± 0.037	Dall'Ora et al. (2014)
SN 2012ec	0.95	0.04	—	—	Barbarino et al. (2015)
SN 2013ab	0.5	0.06	$2.96^{+0.27}_{-2.12}$	0.072 ± 0.036	Bose et al. (2015)

[a] This analysis.

APPENDIX

A. LIGHT-CURVE PARAMETER ESTIMATION

A.1. *Light-Curve Smoothing Algorithm*

The smoothing was performed using a smoothing kernel of the following functional form:

$$K(t, \tau) = N(t, \tau, \sigma(\tau)), \tag{A1}$$

where N is a normal distribution evaluated at time t with mean τ and standard deviation $\sigma(\tau)$ defined by

$$\sigma(\tau) = \begin{cases} 1, & \tau \leq 5 \\ 10, & \tau \geq 50 \\ 0.2\tau, & \text{else}, \end{cases} \tag{A2}$$

where τ is measured in days from explosion. For each time τ, we fit a straight line by solving the least-squares problem

$$f_i = (t_i \ \ 1) \begin{pmatrix} a(\tau) \\ b(\tau) \end{pmatrix} \tag{A3}$$

with weights

$$w_i = K(t_i, \tau, \sigma(\tau))/e_i^2, \tag{A4}$$

where f_i is the flux with error e_i at time t_i. This method has the advantage that it is adaptive to the physically different time scales of the light curve. During the rise, the light curve changes on a short time scale (< 1 day), while during the plateau the time scale is longer (1–2 weeks). We used linear interpolation to fill gaps in the data of greater than 20 days. In addition, we occasionally added auxiliary data points when the smoothed function deviated wildly from a reasonable fit. The resulting smoothed light curves are shown in Figures B6—B9.

A.2. t_0 *from Exponential Fits*

Using a similar parametrization to that of Ofek et al. (2014), we used nonlinear least squares to fit an exponential to the early-time data:

$$f(t) = f_m \left(1 - \exp\left(-\frac{t - t_0}{t_e}\right)\right), \tag{A5}$$

where t is the time in days, f_m is the peak flux, t_0 is the time of explosion, and t_e is the characteristic rise time. The resulting fits are shown in Figure B5. The uncertainties in the parameters were estimated using the 95% confidence levels.

B. EXTENDED DATA
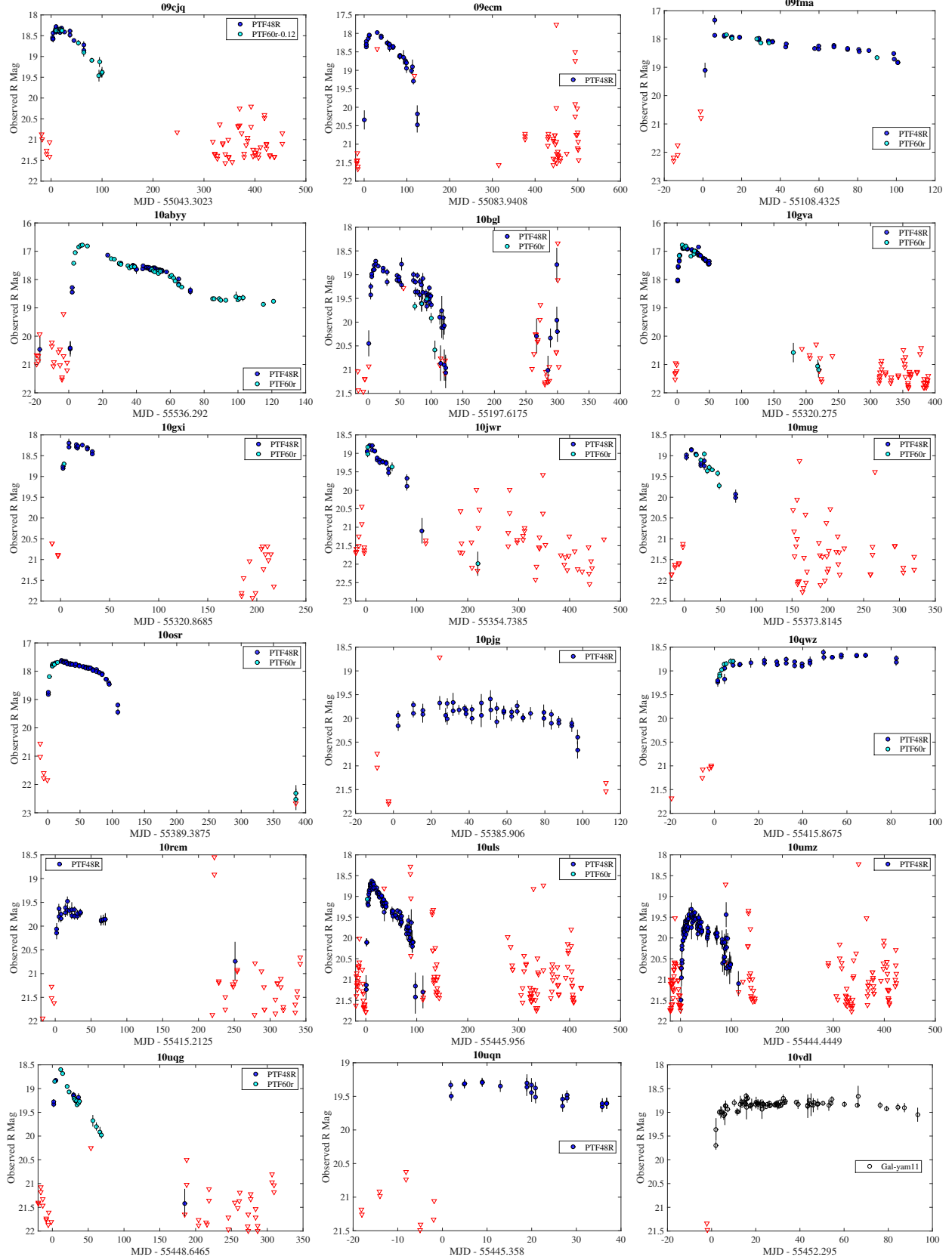
Figure B1. *R*-band light curves. Inverted red triangles represent upper limits. Note that as discussed in the text (Section 3), several have been supplemented with data taken either from the literature (PTF12bvh, iPTF13aaz, PTF10vdl) or from a different telescope (PTF12cod, iPTF13dkk, iPTF13dzb, iPTF13dqy). We have found that small additive constants (indicated in the figures) are needed to make the supplementary data consistent with the PTF observations; this is due most likely to slightly different filter responses.
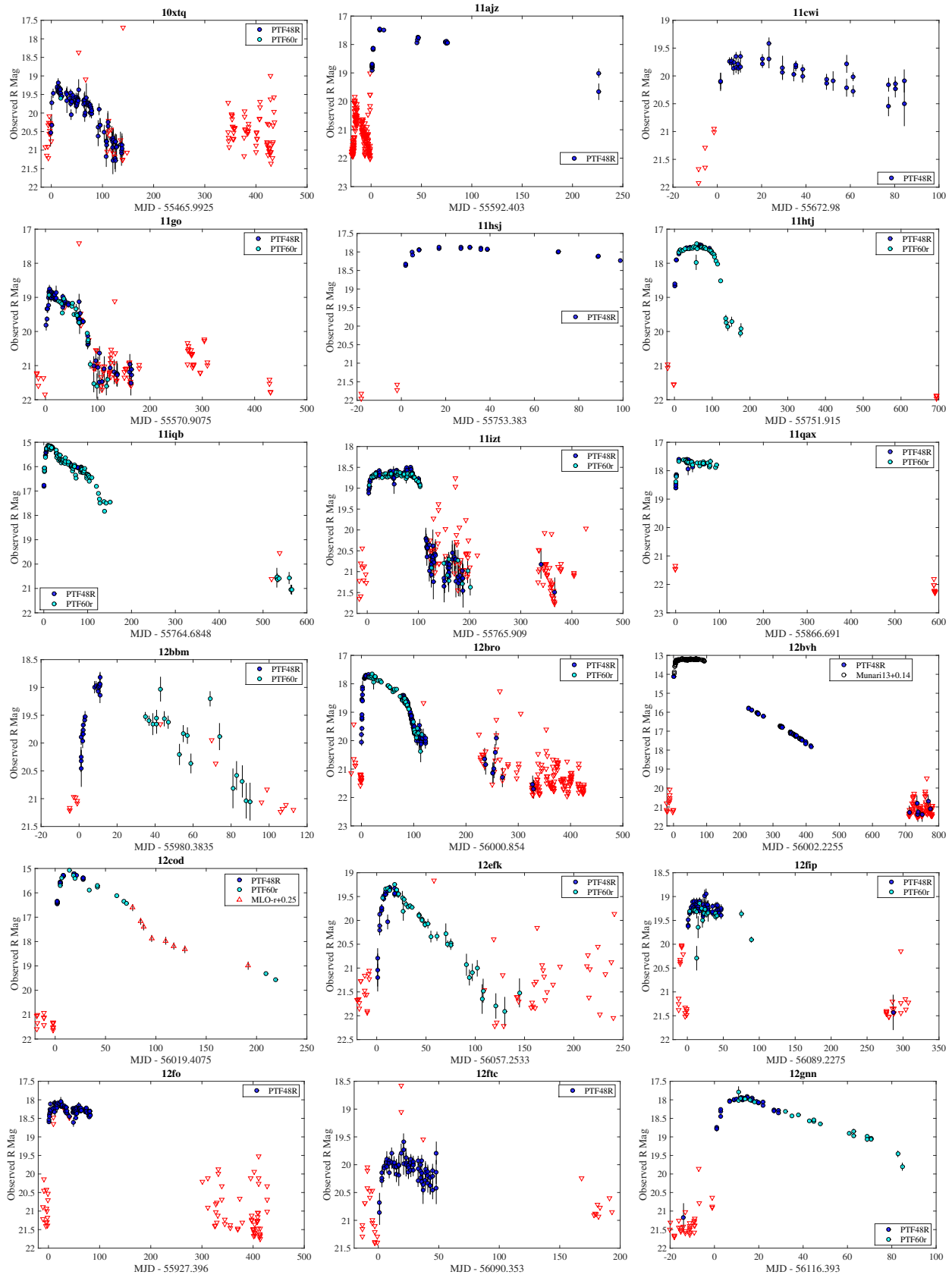
Figure B2. Same as Figure B1.
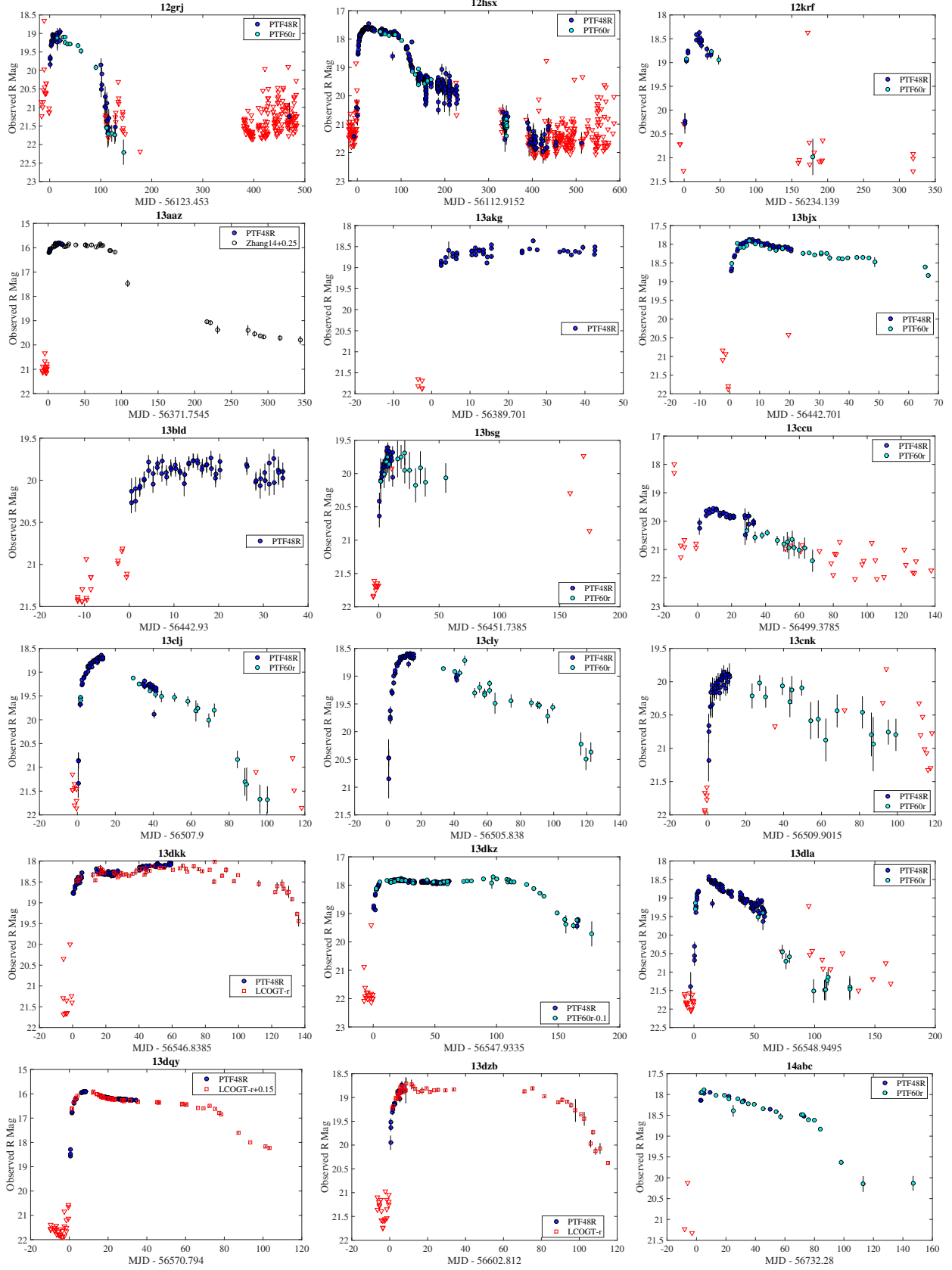
Figure B3. Same as Figure B1.
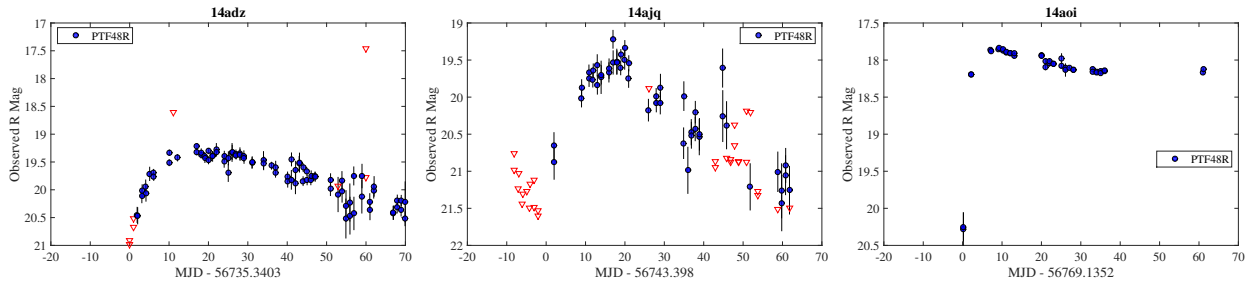
Figure B4. Same as Figure B1.
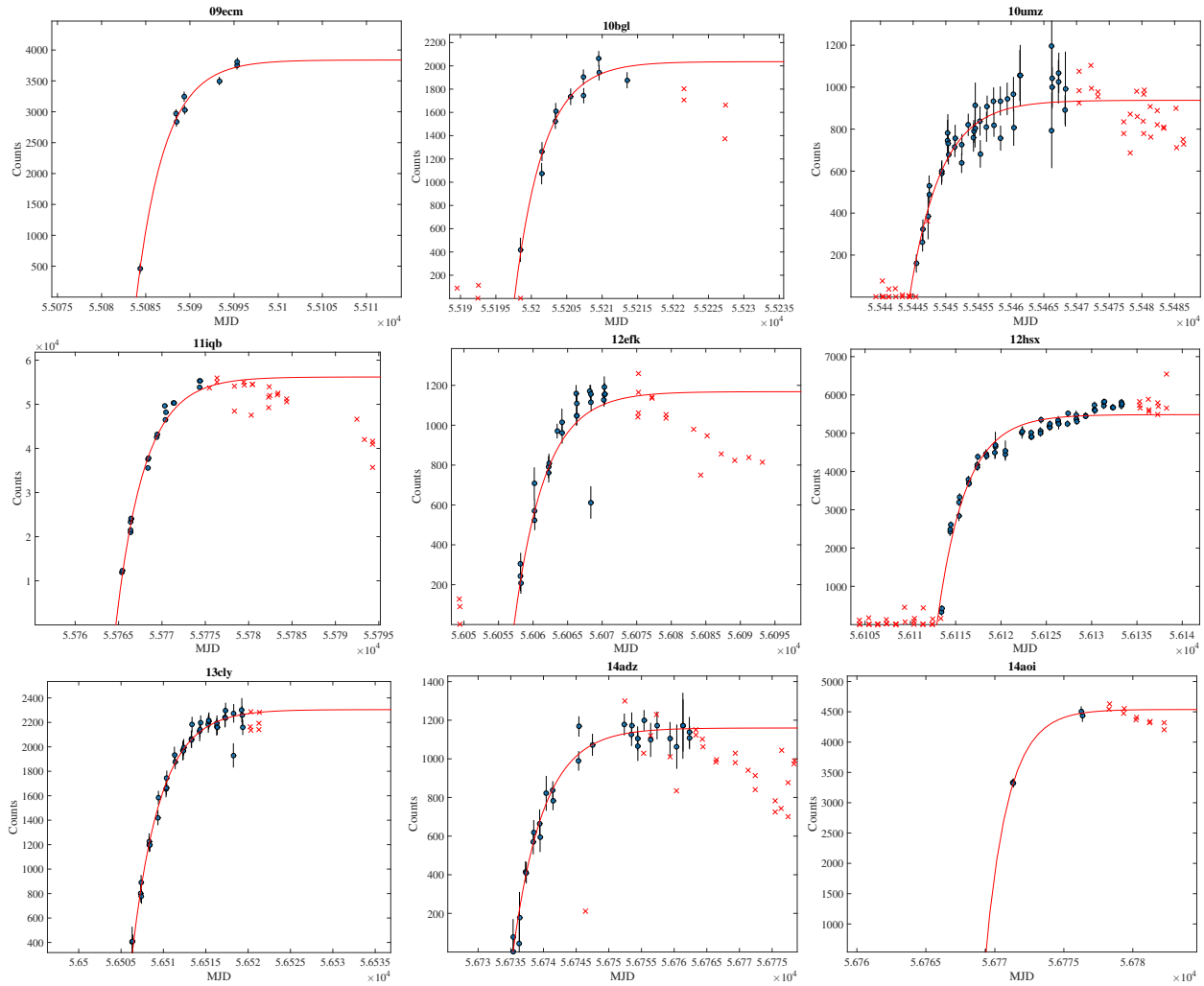
Figure B5. Exponential fits to selected light curves, where limits did not give satisfactory constraints. Red markers were excluded from the fit.
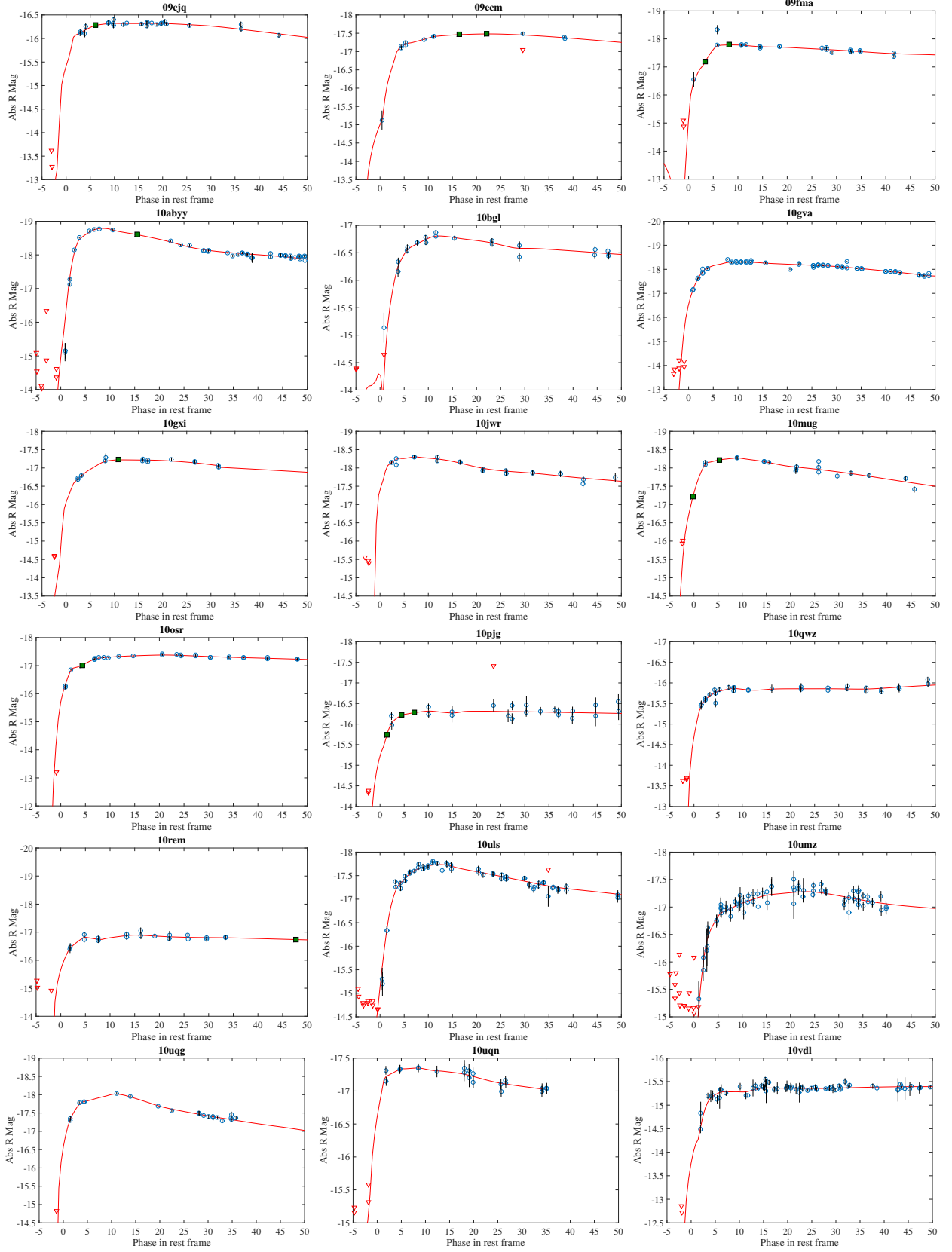
Figure B6. Smoothed R-band light curves. Shown are the data (blue points), auxiliary points defined to improve the interpolation (green squares), and the final smoothed light curve (red solid line).
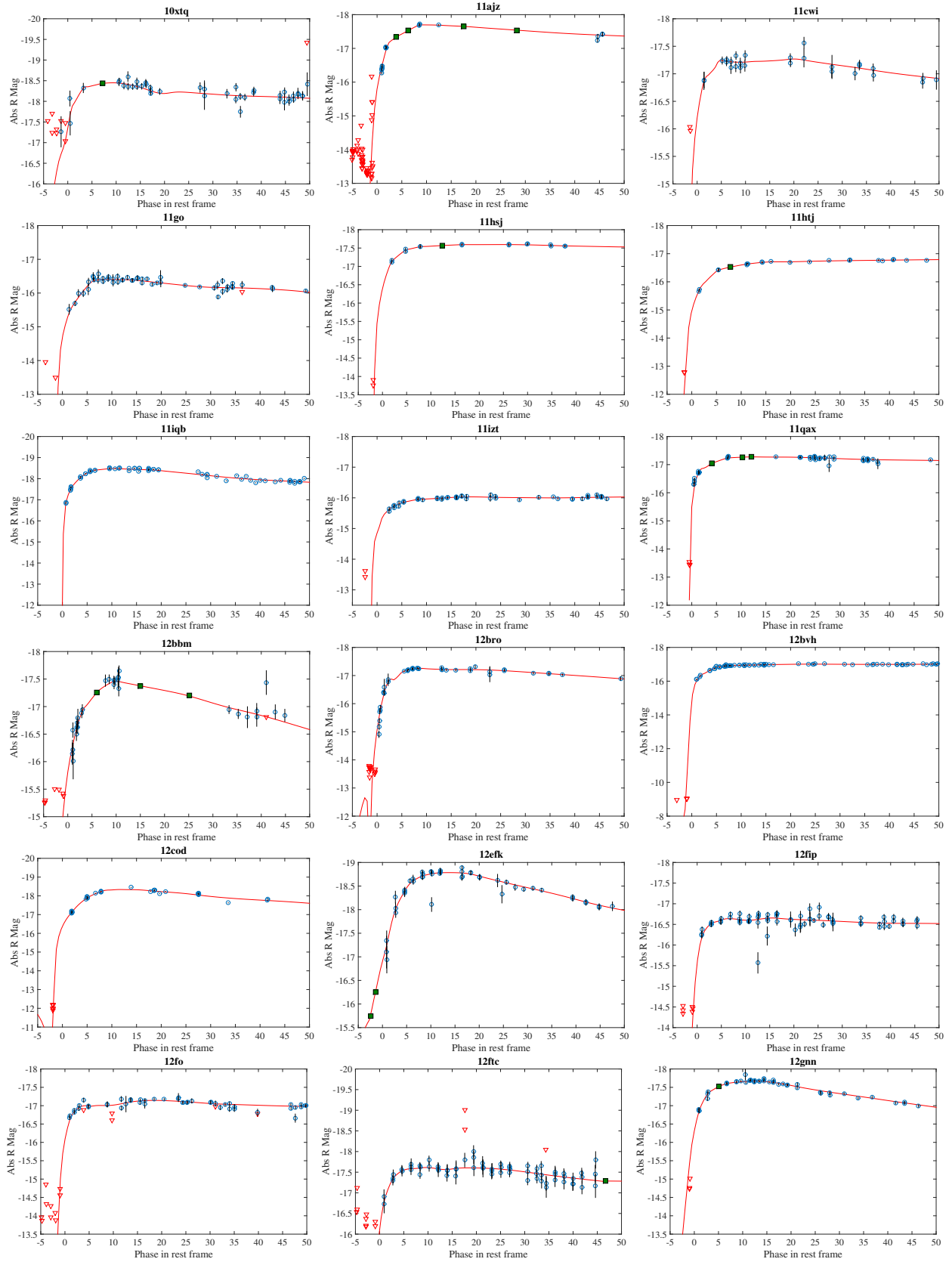
Figure B7. Same as Figure B6.
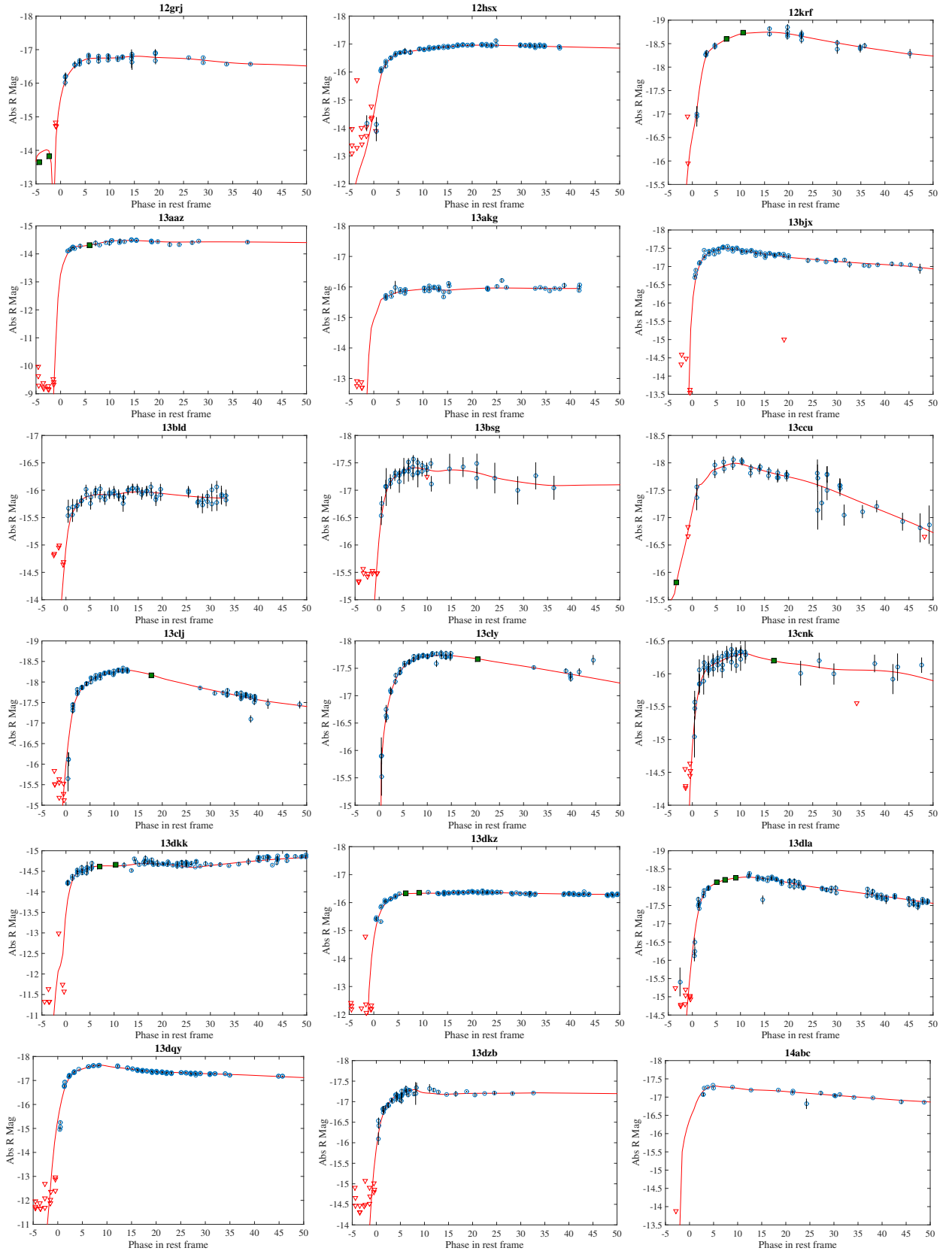
Figure B8. Same as Figure B6.
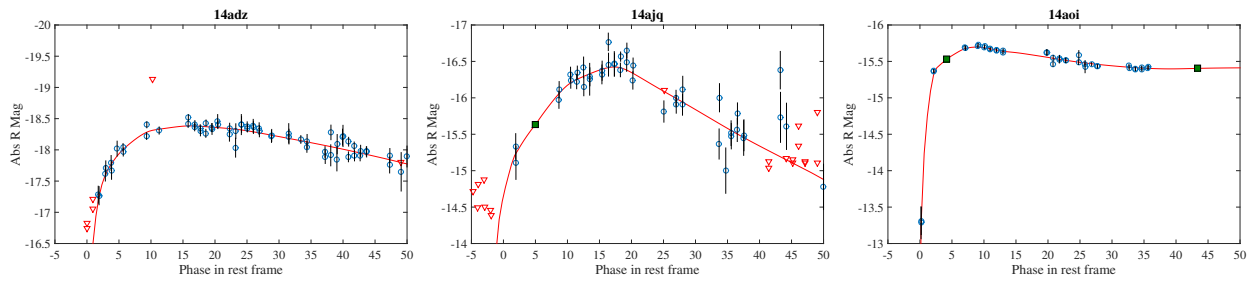
Figure B9. Same as Figure B6.
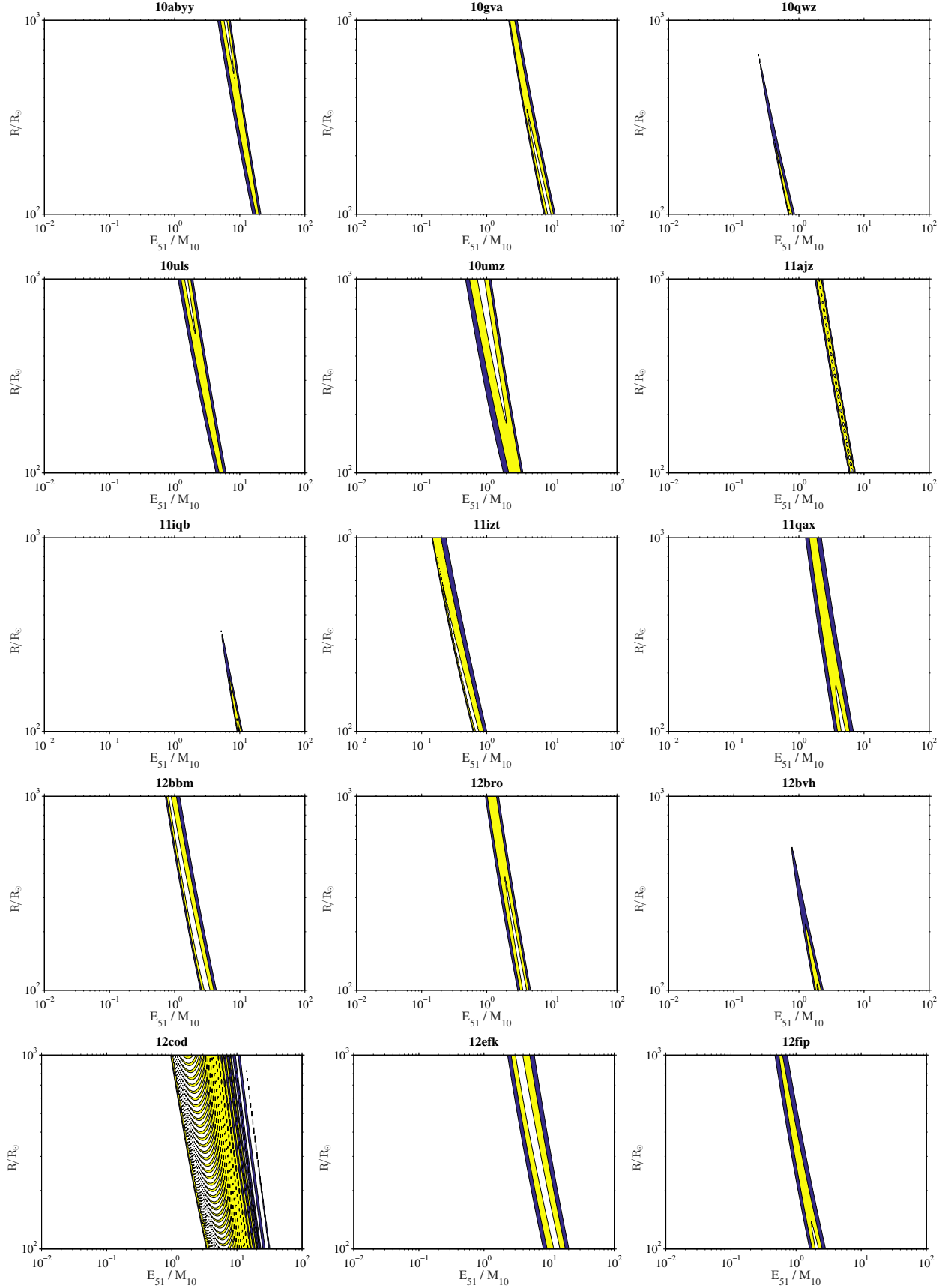
Figure B10. χ^2 of RW11 models for various progenitor radii and E_{51}/M_{10} along the profile of best-fit time of explosion. The white, blue, and teal regions represent the 68%, 95%, and 99.7% confidence regions, respectively.
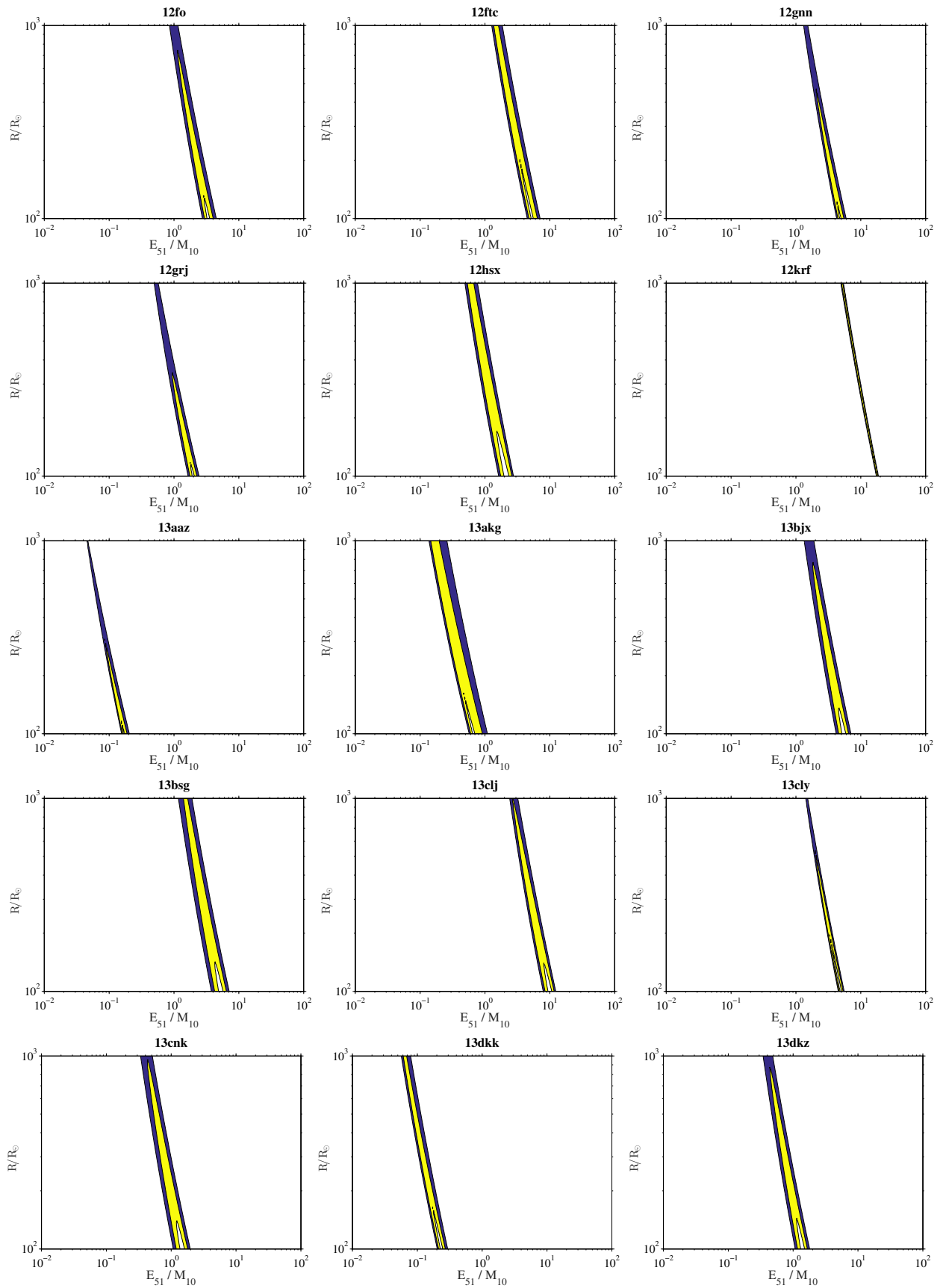
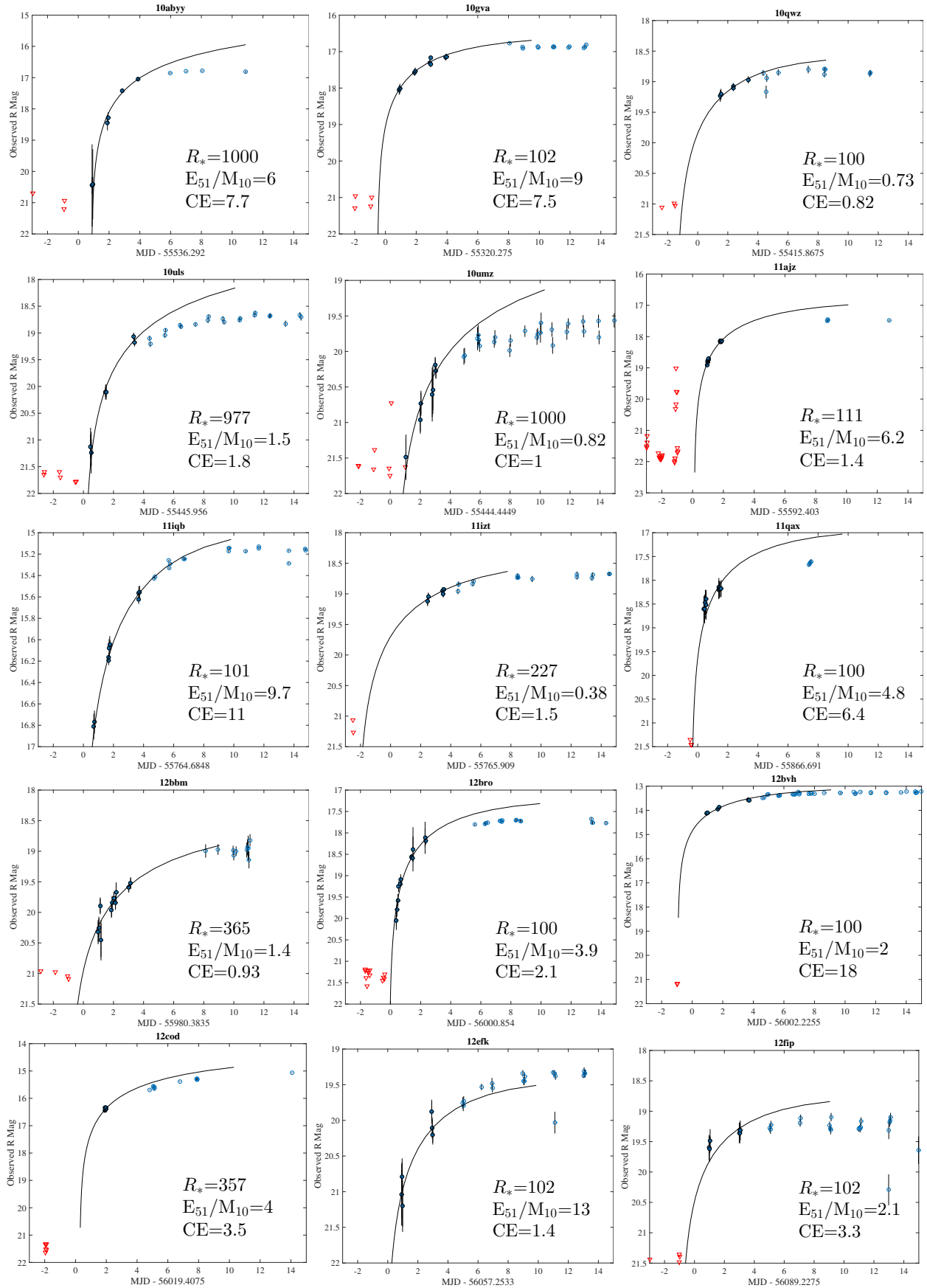**Figure B11.** Same as Figure B10.
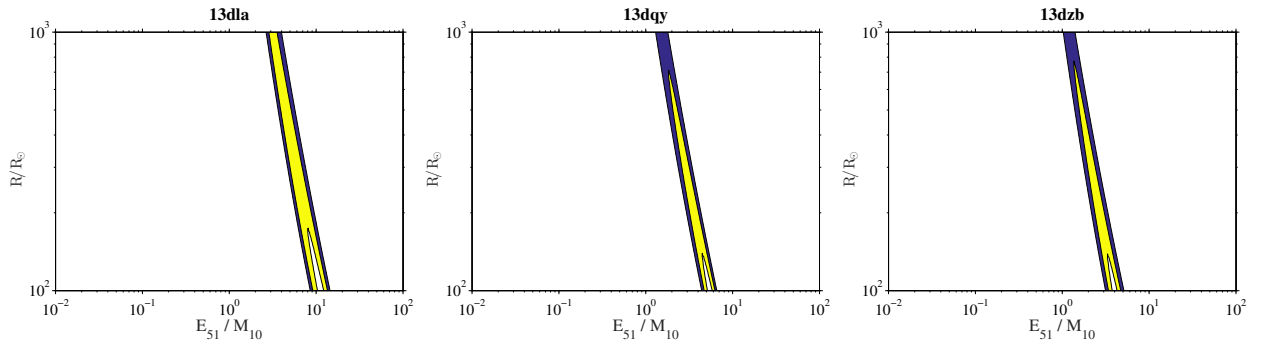
Figure B12. Same as Figure B10.

Figure B13. Best-fit RW11 models to the data. The best-fit radius R_*, energy per unit mass E_{51}/M_{10}, and error scaling factor CE are shown in each figure. Filled symbols are the points that were included in the fit.
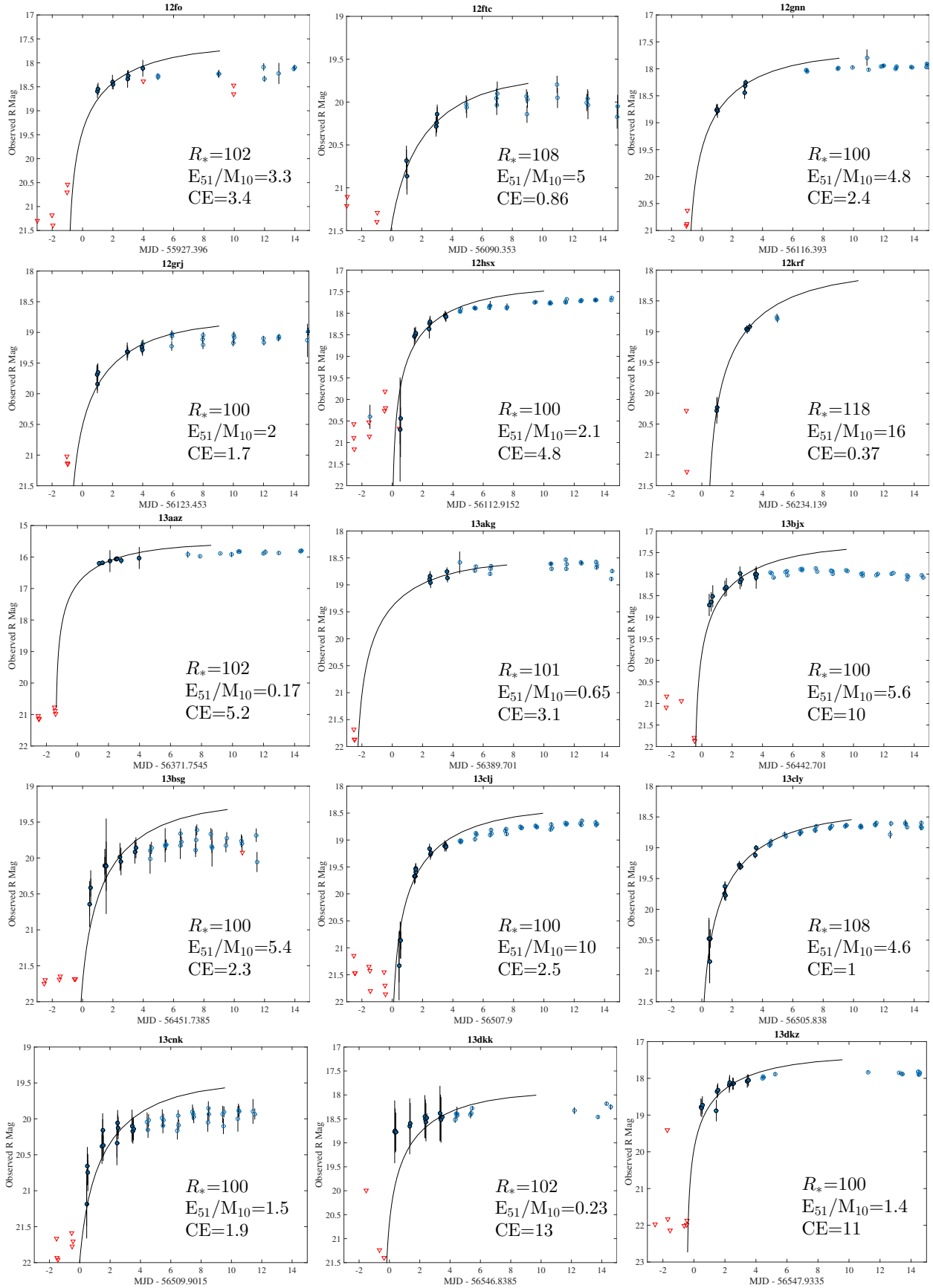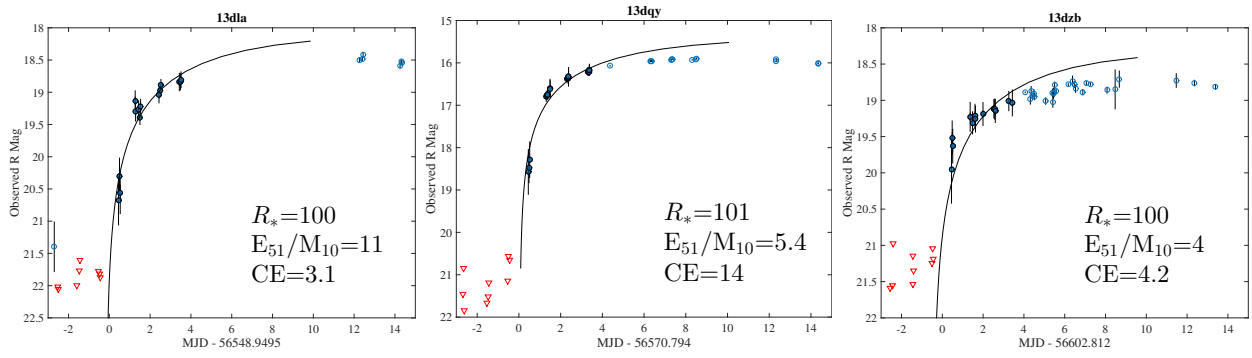
Figure B14. Same as Figure B13.
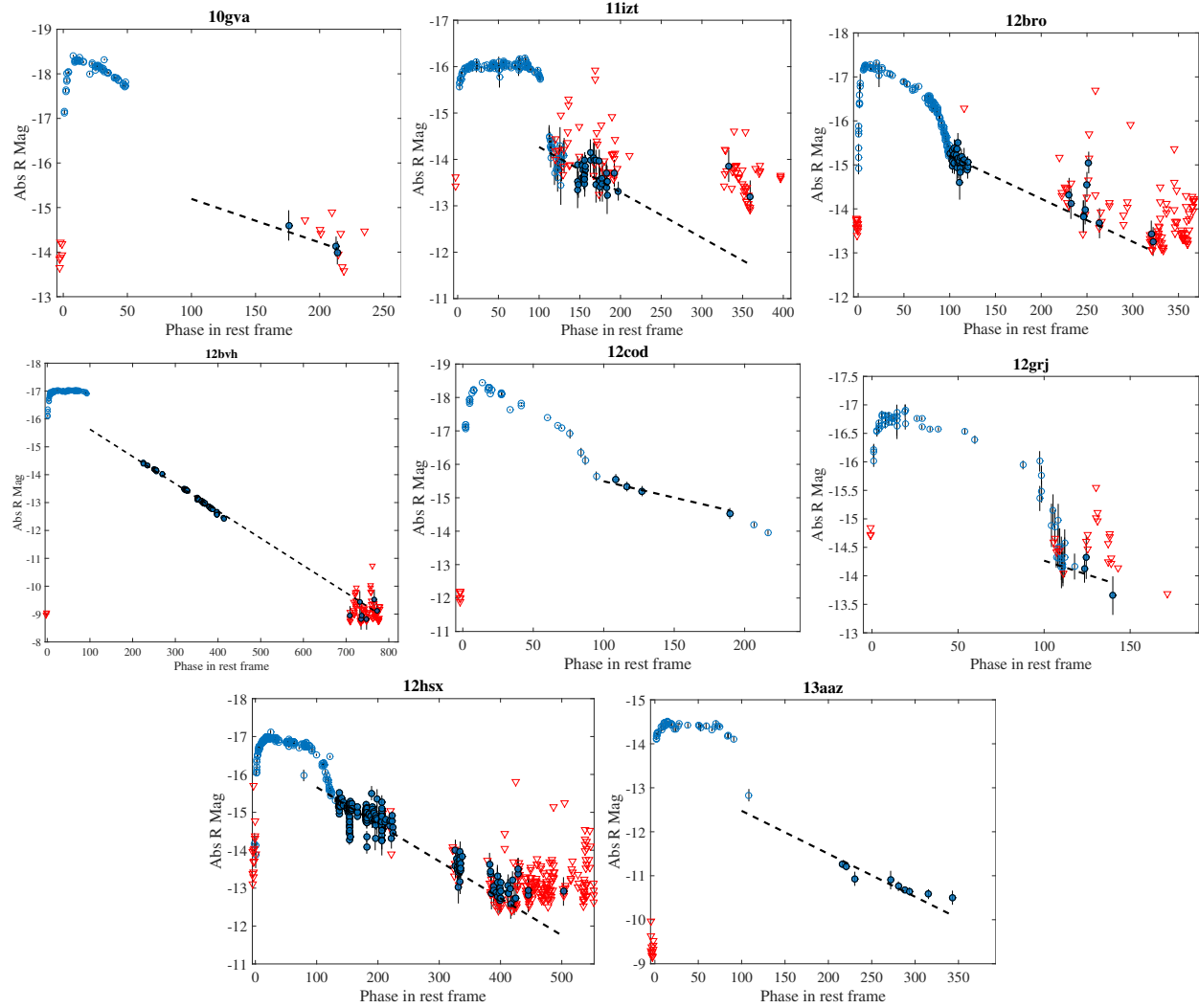
Figure B15. Same as figure B13.

Figure B16. Fits to determine ^{56}Ni mass. Filled symbols have been included in the fit. The dashed line represents the best fit.